

The Luminosity Function of *Fermi*-detected Flat-Spectrum Radio Quasars

M. Ajello^{2,1}, M. S. Shaw^{2,1}, R. W. Romani^{2,1}, C. D. Dermer³, L. Costamante², O. G. King⁴,
W. Max-Moerbeck⁴, A. Readhead⁴, A. Reimer^{5,2}, J. L. Richards⁴, M. Stevenson⁴

ABSTRACT

Fermi has provided the largest sample of γ -ray selected blazars to date. In this work we use a complete sample of FSRQs detected during the first year of operation to determine the luminosity function (LF) and its evolution with cosmic time. The number density of FSRQs grows dramatically up to redshift ~ 0.5 – 2.0 and declines thereafter. The redshift of the peak in the density is luminosity dependent, with more luminous sources peaking at earlier times; thus the LF of γ -ray FSRQs follows a luminosity-dependent density evolution similarly to that of radio-quiet AGN. Also using data from the *Swift* Burst Alert Telescope we derive the average spectral energy distribution of FSRQs in the 10 keV–100 GeV band and show that there is no correlation of the peak γ -ray luminosity with γ -ray peak frequency. The coupling of the SED and LF allows us to predict that the contribution of FSRQs to the *Fermi* isotropic γ -ray background is $9.3^{+1.6}_{-1.0}\%$ ($\pm 3\%$ systematic uncertainty) in the 0.1–100 GeV band. Finally we determine the LF of unbeamed FSRQs, finding that FSRQs have an average Lorentz factor of $\gamma = 11.7^{+3.3}_{-2.2}$, that most are seen within 5° of the jet axis, and that they represent only $\sim 0.1\%$ of the parent population.

Subject headings: cosmology: observations – diffuse radiation – galaxies: active
gamma rays: diffuse background – surveys – galaxies: jets

¹Corresponding authors: M. Ajello, majello@slac.stanford.edu; R. W. Romani, rwr@astro.stanford.edu; M. S. Shaw, msshaw@stanford.edu.

²W. W. Hansen Experimental Physics Laboratory, Kavli Institute for Particle Astrophysics and Cosmology, Department of Physics and SLAC National Accelerator Laboratory, Stanford University, Stanford, CA 94305, USA

³Space Science Division, Naval Research Laboratory, Washington, DC 20375-5352, USA

⁴Cahill Center for Astronomy and Astrophysics, California Institute of Technology, Pasadena, CA 91125, USA

⁵Institut für Astro- und Teilchenphysik and Institut für Theoretische Physik, Leopold-Franzens-Universität Innsbruck, A-6020 Innsbruck, Austria

1. Introduction

The detection of luminous quasars at redshift >6 (e.g. Fan et al. 2003; Willott et al. 2010) provides evidence of super-massive black hole (SMBHs) formation in the first 1 Gyr of cosmic time. There are appreciable challenges to forming (see e.g. Wyithe & Loeb 2003; Volonteri & Rees 2005; Begelman et al. 2006; Mayer et al. 2010) and fueling (see Kauffmann & Haehnelt 2000; Wyithe & Loeb 2003; Croton et al. 2006) these objects at such early times, although it is widely believed that strong accretion can be initiated by major mergers (see Kauffmann & Haehnelt 2000; Wyithe & Loeb 2003; Croton et al. 2006).

Blazars represent an extreme manifestation of such AGN activity, with radiation along the Earth line-of-sight dominated by a relativistic jet. It is, as yet, unclear how such jet activity connects with the more isotropically emitted bulk accretion luminosity. For example according to Blandford & Znajek (1977), the energy stored in a black hole’s spin can be extracted in the form of a relativistic jet. Thus blazar evolution may be connected with the cosmic evolution of the spin states of massive black holes. Radio-loud (jet dominated) blazars have been seen at redshifts as high as $z=5.5$ (Romani 2006), and it is plausible that major mergers, more frequently experienced in the early universe, might preferentially produce maximally rotating black holes (e.g. see Escala et al. 2004; Dotti et al. 2007).

Thus the study of radio-loud (RL) AGN, blazars, with strong relativistically beamed jets can provide a method to study jet activity, BH spin, and major merger events. This can be done by determining the luminosity function of blazars (LF, essentially the number of blazars per comoving volume element within a certain luminosity range) and its evolution with redshift. The *Fermi* Gamma-ray Space Telescope provides one of the largest data sets with which to study the properties of blazars. Thanks to its sensitivity and uniform coverage of the sky, *Fermi* has detected hundreds of blazars from low redshifts out to $z=3.1$ (Abdo A., et al., 2011).

The LF of blazars also allows us to evaluate their contribution to the diffuse backgrounds and to determine their relationship with the parent population (Ajello et al. 2008b; Inoue 2011). Blazars have been extensively studied at radio (Dunlop & Peacock 1990; Wall et al. 2005), soft X-ray (Giommi & Padovani 1994; Rector et al. 2000; Wolter & Celotti 2001; Caccianiga et al. 2002; Beckmann et al. 2003; Padovani et al. 2007) and GeV energies (Hartman et al. 1999). It seems clear that flat spectrum radio quasars (FSRQs) evolve positively (i.e. there were more blazars in the past, Dunlop & Peacock 1990) up to a redshift cut-off which depends on luminosity (e.g. Padovani et al. 2007; Wall 2008; Ajello et al. 2009b). In this respect FSRQs evolve similarly to the population of X-ray selected, radio-quiet, AGNs (Ueda et al. 2003; Hasinger et al. 2005; La Franca et al. 2005). On the other hand, the evolution of the other major class of *Fermi*-detected AGN, BL Lac objects, and their relation

to FSRQs, remains a matter of debate, with claims of no evolution (Caccianiga et al. 2002; Padovani et al. 2007) or even negative evolution (e.g. Rector et al. 2000; Beckmann et al. 2003). Samples with larger redshift completeness fractions are needed to study the LF of these claims.

In this work we report on the LF of FSRQs detected by *Fermi* in its first year of operation. There have been attempts in the past (e.g. Chiang et al. 1995) to characterize the evolution of γ -ray AGN, starting from the EGRET sample (Hartman et al. 1999). One challenge was the small sample size and redshift incompleteness of the EGRET set. Often it was assumed that the γ -ray detected blazars had a LF following that of another band, e.g. radio- or X-ray selected blazars. The results reported in e.g. Stecker & Salamon (1996), Narumoto & Totani (2006), Inoue & Totani (2009), Stecker & Venters (2010) follow this approach. Alternatively, a LF may be estimated from the γ -ray sample directly (Chiang & Mukherjee 1998; Mücke & Pohl 2000; Dermer 2007; Bhattacharya et al. 2009), although only a small (~ 60) blazar sample including both BL Lac objects and FSRQs was available (from EGRET data) with acceptable incompleteness.

We report here on a detailed LF measured from a sample of 186 γ -ray selected FSRQs detected by *Fermi*. The work is organized as follows. Sections 2 and 3 describe the properties of the sample used and the method employed to determine the LF of blazars. The luminosity function of FSRQs is derived in Section 4. In Section 5 the spectral energy distributions (SEDs) of *Fermi*'s FSRQs are analyzed in detail, testing for possible correlations of the peak energy with the peak luminosity. The contribution of FSRQs to the isotropic gamma-ray background¹(IGRB, see Abdo et al. 2010d) is determined and discussed in Section 6. Throughout this paper, we assume a standard concordance cosmology ($H_0=71 \text{ km s}^{-1} \text{ Mpc}^{-1}$, $\Omega_M=1-\Omega_\Lambda=0.27$).

2. The Sample

The First Fermi LAT Catalog (1FGL, Abdo et al. 2010a) reports on more than 1400 sources detected by *Fermi*-LAT during its first year of operation. The first LAT AGN catalog (1LAC, Abdo et al. 2010f) associates ~ 700 of the high-latitude 1FGL sources ($|b| \geq 10^\circ$) with AGN of various types, most of which are blazars. The sample used for this analysis consists of sources detected by the pipeline developed by Abdo et al. (2010e) with a test

¹The isotropic gamma-ray background refers to the isotropic component of the *Fermi* sky (Abdo et al. 2010d) and as such might include components generated locally (e.g. Keshet et al. 2004) and components of truly extragalactic origin.

statistic (TS) significance greater than 50 and with $|b| \geq 15^\circ$. For these sample cuts we have produced a set of Monte Carlo simulations that can be used to determine and account for the selection effects. This sample contains 483 objects, 186 of which are classified as FSRQs. The faintest identified FSRQ has a 100 MeV – 100 GeV band flux of $F_{100} \approx 10^{-8} \text{ ph cm}^{-2} \text{ s}^{-1}$. To limit the incompleteness (i.e. the fraction of sources without an association) we apply this as a flux limit to the sample of 483 objects, resulting in a full sample of 433 sources of which 29 (i.e. $\sim 7\%$) do not have associated counterparts.

The composition of this sample is reported in Table 1. The 186 FSRQs detected by *Fermi* with $\text{TS} \geq 50$, $|b| \geq 15^\circ$, and $F_{100} \geq 10^{-8} \text{ ph cm}^{-2} \text{ s}^{-1}$ constitute the sample that will be used in this analysis.

3. Method

A classical approach to derive the LF is based on the $1/V_{\text{MAX}}$ method of Schmidt (1968) applied to redshift bins. However, this method is known to introduce bias if there is significant evolution within the bins. Moreover, given our relatively small sample size and the large volume and luminosity range spanned, binning would result in a loss of information. Thus we decided to apply the maximum-likelihood (ML) algorithm first introduced by Marshall et al. (1983) and used recently by Ajello et al. (2009b) for the study of blazars detected by *Swift*. The aim of this analysis is to determine the space density of FSRQs as a function of rest-frame 0.1–100 GeV luminosity (L_γ), redshift (z) and photon index (Γ), by fitting to the functional form

$$\frac{d^3N}{dL_\gamma dz d\Gamma} = \frac{d^2N}{dL_\gamma dV} \times \frac{dN}{d\Gamma} \times \frac{dV}{dz} = \Phi(L_\gamma, z) \times \frac{dN}{d\Gamma} \times \frac{dV}{dz} \quad (1)$$

where $\Phi(L_\gamma, z)$ is the luminosity function, and dV/dz is the co-moving volume element per unit redshift and unit solid angle (see e.g. Hogg 1999). The function $dN/d\Gamma$ is the (intrinsic) photon index distribution and is assumed to be independent of z . It is modeled as a Gaussian:

$$\frac{dN}{d\Gamma} = e^{-\frac{(\Gamma-\mu)^2}{2\sigma^2}} \quad (2)$$

where μ and σ are respectively the mean and the dispersion of the Gaussian distribution.

The best-fit LF is found by comparing, through a maximum-likelihood estimator, the number of expected objects (for a given model LF) to the observed number while accounting for selection effects in the survey. In this method, the space of luminosity, redshift, and photon index is divided into small intervals of size $dL_\gamma dz d\Gamma$. In each element, the expected

Table 1. Composition of the $|b| \geq 15^\circ$, $TS \geq 50$, $F_{100} \geq 10^{-8}$ ph cm $^{-2}$ s $^{-1}$ sample used in this analysis.

CLASS	# objects
Total	433
FSRQs	186
BL Lacs	157
Pulsars	28
Other ^a	16
Radio Associations ^b	17
Unassociated sources	29

^aIncludes starburst galaxies, LINERS, narrow line Seyfert 1 objects and Seyfert galaxy candidates.

^b*Fermi* sources with a radio counterpart, but no optical type or redshift measurement.

number of blazars with luminosity L_γ , redshift z and photon index Γ is:

$$\lambda(L_\gamma, z, \Gamma)dL_\gamma dz d\Gamma = \Phi(L_\gamma, z)\Omega(L_\gamma, z, \Gamma)\frac{dN}{d\Gamma}\frac{dV}{dz}dL_\gamma dz d\Gamma \quad (3)$$

where $\Omega(L_\gamma, z, \Gamma)$ is the sky coverage and represents the probability of detecting in this survey a blazar with luminosity L_γ , redshift z and photon index Γ . This probability was derived for the sample used here by Abdo et al. (2010e) and the reader is referred to that aforementioned paper for more details. With sufficiently fine sampling of the $L_\gamma - z - \Gamma$ space the infinitesimal element will either contain 0 or 1 FSRQs. In this regime one has a likelihood function based on joint Poisson probabilities:

$$L = \prod_i \lambda(L_{\gamma,i}, z_i, \Gamma_i)dL_\gamma dz d\Gamma e^{-\lambda(L_{\gamma,i}, z_i, \Gamma_i)dL_\gamma dz d\Gamma} \times \prod_j e^{-\lambda(L_{\gamma,j}, z_j, \Gamma_j)dL_\gamma dz d\Gamma} \quad (4)$$

This is the combined probability of observing one blazar in each bin of $(L_{\gamma,i}, z_i, \Gamma_i)$ populated by one *Fermi* FSRQ and zero FSRQs for all other $(L_{\gamma,j}, z_j, \Gamma_j)$. Transforming to the standard expression $S = -2 \ln L$ and dropping terms which are not model dependent, we obtain:

$$S = -2 \sum_i \ln \frac{d^3 N}{dL_\gamma dz d\Gamma} + 2 \int_{\Gamma_{min}}^{\Gamma_{max}} \int_{L_{\gamma,min}}^{L_{\gamma,max}} \int_{z_{min}}^{z_{max}} \lambda(L_\gamma, \Gamma, z) dL_\gamma dz d\Gamma \quad (5)$$

The limits of integration of Eq. 5, unless otherwise stated, are: $L_{\gamma,min}=10^{44}$ erg s⁻¹, $L_{\gamma,max}=10^{52}$ erg s⁻¹, $z_{min}=0$, $z_{max}=6$, $\Gamma_{min}=1.8$ and $\Gamma_{max}=3.0$. The best-fit parameters are determined by minimizing² S and the associated 1σ error are computed by varying the parameter of interest, while the others are allowed to float, until an increment of $\Delta S=1$ is achieved. This gives an estimate of the 68% confidence region for the parameter of interest (Avni 1976). While computationally intensive, Eq. 5 has the advantage that each source has its appropriate individual detection efficiency and k-correction treated independently.

In order to test whether the best-fit LF provides a good description of the data we compare the *observed* redshift, luminosity, index and source count distributions against the prediction of the LF. The first three distributions can be obtained from the LF as:

$$\frac{dN}{dz} = \int_{\Gamma_{min}}^{\Gamma_{max}} \int_{L_{\gamma,min}}^{L_{\gamma,max}} \lambda(L_\gamma, \Gamma, z) dL_\gamma d\Gamma \quad (6)$$

$$\frac{dN}{dL_\gamma} = \int_{\Gamma_{min}}^{\Gamma_{max}} \int_{z_{min}}^{z_{max}} \lambda(L_\gamma, \Gamma, z) dz d\Gamma \quad (7)$$

$$\frac{dN}{d\Gamma} = \int_{L_{\gamma,min}}^{L_{\gamma,max}} \int_{z_{min}}^{z_{max}} \lambda(L_\gamma, \Gamma, z) dL_\gamma dz \quad (8)$$

²The MINUIT minimization package, embedded in ROOT (root.cern.ch), has been used for this purpose.

where the extremes of integrations are the same as in Eq. 5. The source count distribution can be derived as :

$$N(> S) = \int_{\Gamma_{min}}^{\Gamma_{max}} \int_{z_{min}}^{z_{max}} \int_{L_{\gamma}(z,S)}^{L_{\gamma,max}} \Phi(L_{\gamma,z}) \frac{dN}{d\Gamma} \frac{dV}{dz} d\Gamma dz dL_{\gamma} \quad (9)$$

where $L_{\gamma}(z, S)$ is the luminosity of a source at redshift z having a flux of S .

To display the LF we rely on the “ N^{obs}/N^{mdl} ” method devised by La Franca & Cristiani (1997) and Miyaji et al. (2001) and employed in several recent works (e.g. La Franca et al. 2005; Hasinger et al. 2005). Once a best-fit function for the LF has been found, it is possible to determine the value of the observed LF in a given bin of luminosity and redshift:

$$\Phi(L_{\gamma,i}, z_i) = \Phi^{mdl}(L_{\gamma,i}, z_i) \frac{N_i^{obs}}{N_i^{mdl}} \quad (10)$$

where $L_{\gamma,i}$ and z_i are the luminosity and redshift of the i^{th} bin, $\Phi^{mdl}(L_{\gamma,i}, z_i)$ is the best-fit LF model and N_i^{obs} and N_i^{mdl} are the observed and the predicted number of FSRQs in that bin. These two techniques (the Marshall et al. (1983) ML method and the “ N^{obs}/N^{mdl} ” estimator) provide a minimally biased estimate of the luminosity function, (cf. Miyaji et al. 2001).

4. Results

4.1. Pure Luminosity Evolution and the Evidence for a Redshift Peak

The space density of radio-quiet AGNs is known to be maximal at intermediate redshift. The epoch of this ‘redshift peak’ correlates with source luminosity (e.g. Ueda et al. 2003; Hasinger et al. 2005). This peak may represent the combined effect of SMBH growth over cosmic time and a fall-off in fueling activity as the rate of major mergers decreases at late times. To test whether such behavior is also typical of the LAT FSRQ population, we perform a fit to the data using a pure luminosity evolution (PLE) model of the form:

$$\Phi(L_{\gamma}, z) = \Phi(L_{\gamma}/e(z)) \quad (11)$$

where

$$\Phi(L_{\gamma}/e(z=0)) = \frac{dN}{dL_{\gamma}} = \frac{A}{\ln(10)L_{\gamma}} \left[\left(\frac{L_{\gamma}}{L_*} \right)^{\gamma_1} + \left(\frac{L_{\gamma}}{L_*} \right)^{\gamma_2} \right]^{-1} \quad (12)$$

and

$$e(z) = (1+z)^k e^{z/\xi}. \quad (13)$$

In this model the evolution is entirely in luminosity: i.e. the FSRQ were more luminous in the past if positive evolution ($k > 0$) is found (the opposite is true otherwise). It is also straightforward to demonstrate that the luminosity evolution (i.e. Eq. 13) of FSRQs peaks at $z_c = -1 - k\xi$. The best-fit parameters are reported in Table 2. The evolution of the FSRQ class is found to be positive and fast ($k = 5.70 \pm 1.02$). The redshift peak is $z_c = 1.62 \pm 0.03$. Moreover, the subsequent rate of decrease of the luminosity after the peak is well constrained ($\xi = -0.46 \pm 0.01$). However, as shown in Fig. 1, while this model provides a good fit to the observed redshift and luminosity distributions, it is a very poor representation of the measured $\log N$ – $\log S$.

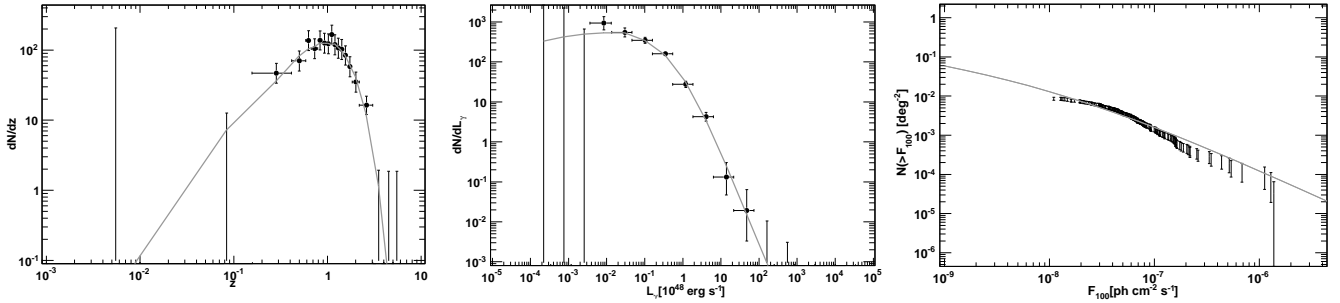


Fig. 1.— Redshift (left), luminosity (middle) and source count (right) distribution of LAT FSRQs. The dashed line is the best-fit PLE model discussed in the text.

We next test whether the redshift peak depends on luminosity, splitting the data set at $L_\gamma = 3.2 \times 10^{47} \text{ erg s}^{-1}$. A fit is then performed to each sub-sample to determine the position of the redshift peak (if any), keeping the parameters of Eq. 12 fixed. The results of the fits to the low- and high-luminosity data sets are reported in Table 2. From Eq. 13 and the values of k and ξ it is apparent that there is a significant shift in the redshift peak, with the low- and high- luminosity samples peaking at ~ 1.15 and ~ 1.77 , respectively.

Table 2. Best-fit parameters of the Pure Luminosity Evolution LF. Parameters without an error estimate were kept fixed during the fit.

Sample	# Objects	A ^a	γ_1	L_*	γ_2	k	ξ	μ	σ
ALL	186	$5.59(\pm 0.41) \times 10^3$	0.29 ± 0.53	0.026 ± 0.066	1.25 ± 0.32	5.70 ± 1.02	-0.46 ± 0.01	2.45 ± 0.13	0.18 ± 0.01
Low L	89	$15.4(\pm 0.2) \times 10^3$	0.29	0.026	1.25	4.30 ± 2.39	-0.50 ± 0.04	2.47 ± 0.04	0.21 ± 0.03
High L	97	$22.6(\pm 2.0) \times 10^3$	0.29	0.026	1.25	3.47 ± 1.73	-0.79 ± 0.04	2.46 ± 0.02	0.20 ± 0.02

^aIn unit of $10^{-13} \text{ Mpc}^{-3} \text{ erg}^{-1} \text{ s}$.

4.2. The Luminosity Dependent Density Evolution and the Redshift Peak

Since a simple PLE LF model provides an inadequate fit to the *Fermi* data and since there is some evidence for the evolution of the redshift peak with luminosity, we now fit the *Fermi* FSRQ set to a luminosity-dependent density evolution model (LDDE). Here the evolution is primarily in density with a luminosity-dependent redshift peak. The LDDE model is parametrized

$$\Phi(L_\gamma, z) = \Phi(L_\gamma) \times e(z, L_\gamma) \quad (14)$$

where

$$e(z, L_\gamma) = \left[\left(\frac{1+z}{1+z_c(L_\gamma)} \right)^{p_1} + \left(\frac{1+z}{1+z_c(L_\gamma)} \right)^{p_2} \right]^{-1} \quad (15)$$

and

$$z_c(L_\gamma) = z_c^* \cdot (L_\gamma/10^{48})^\alpha. \quad (16)$$

$\Phi(L_\gamma)$ is the same double power law used in Eq. 12. This parametrization is similar to that proposed by Ueda et al. (2003), but is continuous around the redshift peak $z_c(L_\gamma)$. This has obvious advantages for fitting algorithms that rely on the derivatives of the fitting function to find the minimum. Here $z_c(L_\gamma)$ corresponds to the (luminosity-dependent) redshift where the evolution changes sign (positive to negative), with z_c^* being the redshift peak for a FSRQ with a luminosity of $10^{48} \text{ erg s}^{-1}$.

The LDDE model provides a good fit to the LAT data and is able to reproduce the observed distribution in Fig. 2. The log-likelihood ratio test shows that the improvement over the best PLE model is significant, with a chance probability of $\sim 10^{-6}$. Results are reported in Table 3.

In Fig. 3 we subdivide the sample into four redshift bins with comparable number of sources to illustrate how the LF changes. The evolution, visible as a shifting of the peak and a change of the shape of the LF between different bins of redshift, is clearly visible. This evolution takes place mostly below redshift ~ 1.1 where the space density of our least luminous objects (i.e. $L_\gamma \approx 10^{46} \text{ erg s}^{-1}$) increases by $\sim 10\times$. Above this redshift the variation is less marked, but one notices that:

- the space density of $\log L=47$ objects decreases from redshift 1 to redshift 1.5 while that of $\log L=48$ FSRQs still increases (lower left panel, green versus red line). This indicates that the space density of $\log L=47$ FSRQs peaks at a redshift ~ 1.1 .
- similar behavior holds for $\log L=48$ FSRQs in the highest redshift bin so that their maximum space density should occur well below $z=3$.

The best-fit parameters confirm that the redshift of maximum space density increases with increasing luminosity (with the power-law index of the redshift-peak evolution $\alpha = 0.21 \pm 0.03$, see Eq. 16). This redshift evolution can be clearly seen in Fig. 4, which shows the change in space density for different luminosity classes.

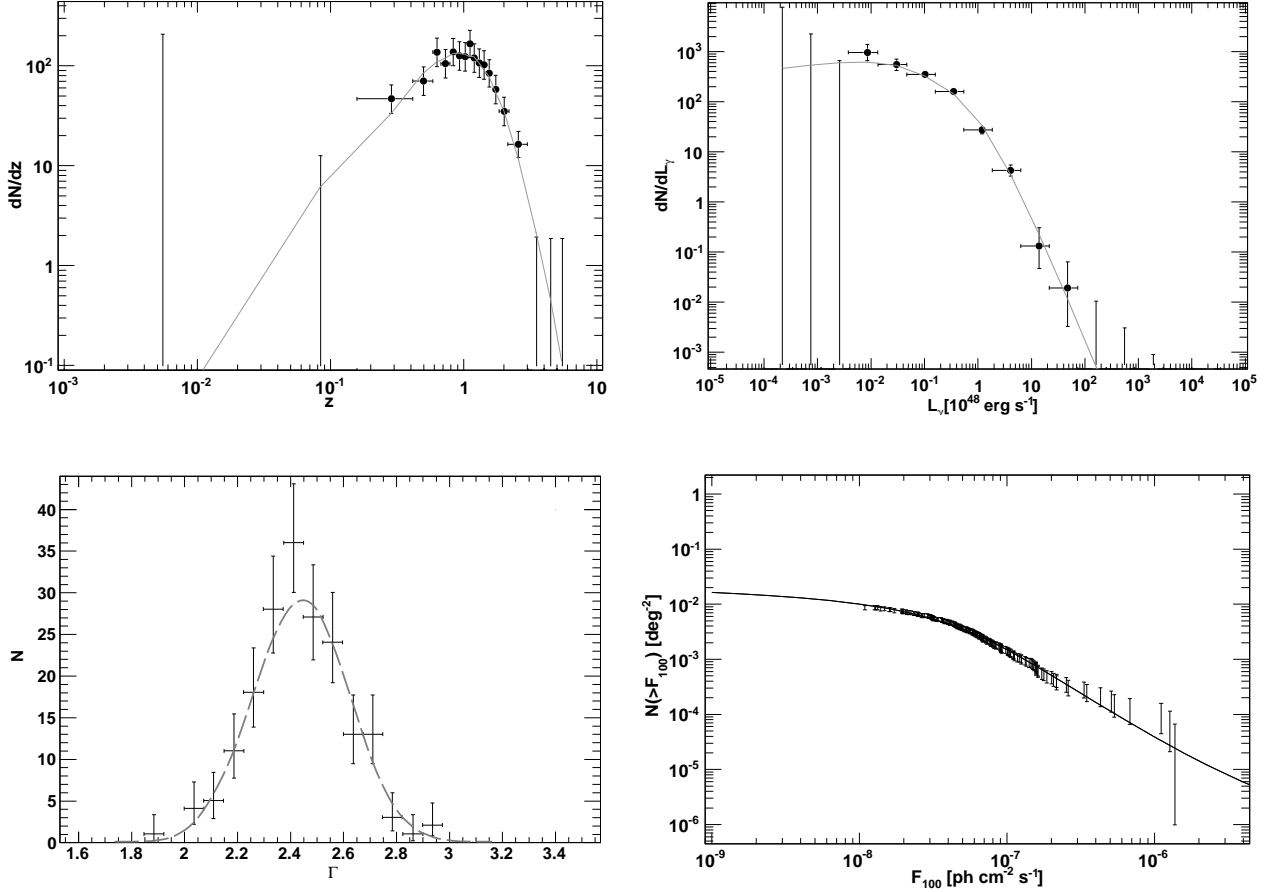


Fig. 2.— Redshift (upper left), luminosity (upper right), photon index (lower left), and source count (lower right) distributions of LAT FSRQs. The dashed line is the best-fit LDDE model convolved with the selection effects of *Fermi*. Notice the greatly improved source count distribution over the predictions of the PLE model of Figure 1.

Table 3. Best-fit parameters of the Luminosity Dependent Density Evolution LF

Sample	# Objects	A ^a	γ_1	L*	γ_2	z_c^*	α	p1	p2	μ	σ
ALL	186	$3.06(\pm 0.23) \times 10^4$	0.21 ± 0.12	0.84 ± 0.49	1.58 ± 0.27	1.47 ± 0.16	0.21 ± 0.03	7.35 ± 1.74	-6.51 ± 1.97	2.44 ± 0.01	0.18 ± 0.01
ALL ^b	208	$2.82(\pm 0.19) \times 10^4$	0.26 ± 0.12	0.87 ± 0.53	1.60 ± 0.27	1.42 ± 0.15	0.20 ± 0.03	8.21 ± 1.78	-5.66 ± 1.73	2.42 ± 0.01	0.19 ± 0.01
ALL ^c	186	$8.72(\pm 0.63) \times 10^3$	0.38 ± 0.16	0.89 ± 0.70	1.60 ± 0.30	1.38 ± 0.18	0.18 ± 0.03	7.71 ± 1.84	-4.44 ± 1.78

^aIn unit of $10^{-13} \text{ Mpc}^{-3} \text{ erg}^{-1} \text{ s}$.

^b22 unassociated sources were included in this sample by drawing random redshifts from the observed redshift distribution of FSRQs.

^cDerived using the detection efficiency for curved reported in Fig. 16

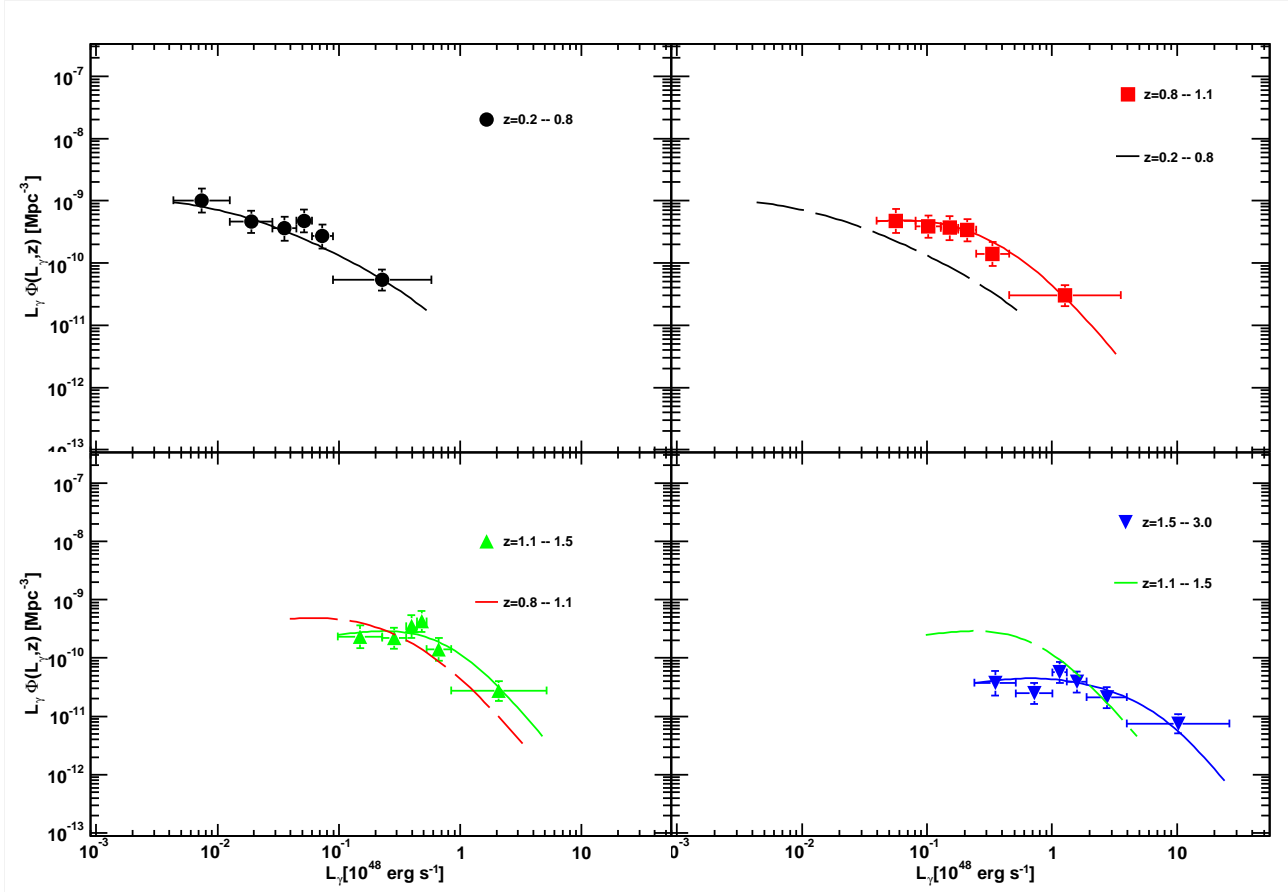


Fig. 3.— LF of the *Fermi* FSRQs in different bins of redshift, reconstructed using the N_{obs}/N_{mdl} method. The lines represent the best-fit LDDE model of § 4.2. To highlight the evolution, the LF from the next lower redshift bin is over-plotted (dashed lines).

4.3. Analysis of Uncertainties

One of the main uncertainties of our analysis is due to the incompleteness of the FSRQ sample. In Table 1, there are 17 sources with associated radio counterparts lacking optical type and redshift measurements. A fraction of these may be FSRQs. In addition, there are 29 sources without any statistically associated radio counterpart. The lack of radio flux means that these cannot be FSRQ similar to those in the *Fermi* sample, unless position errors have prevented radio counterpart associations. Thus even if a few of these sources are mis-localized, the maximum possible incompleteness of our FSRQ sample is on the order of $20/(186+20)$, i.e. $\sim 10\%$.

The standard way to account for this incompleteness is to correct upwards the normal-

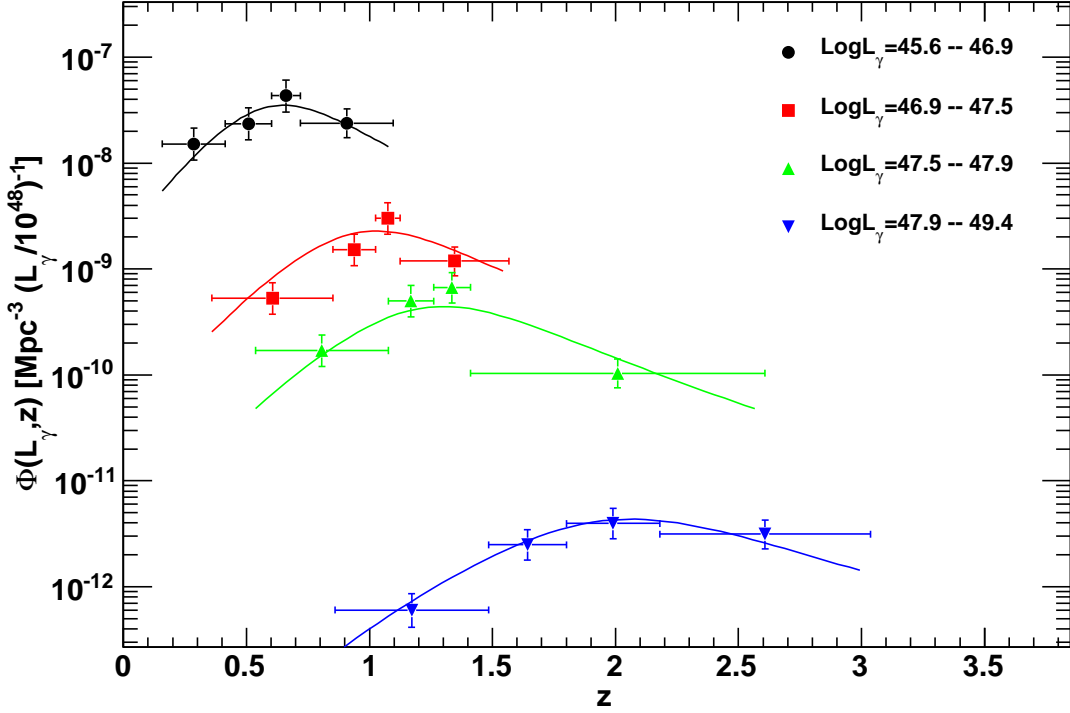


Fig. 4.— Growth and evolution of different luminosity classes of FSRQs. Note that the space density of the most luminous FSRQs peaks earlier in the history of the Universe while the bulk of the population (i.e. the low luminosity objects) are more abundant at later times. The range of measured distribution is determined by requiring at least one source within the volume (lower left) and sensitivity limitations of *Fermi* (upper right).

ization of the LF as to reflect the *likely* real number of FSRQs (associated or not) in our sample. Considering extra information about these sources, this likely incompleteness is even smaller than the 10% above. First, we find that only 50% of all the radio-loud identified sources in our sample are FSRQs. This suggests that only 8 of the 17 radio identified sources are FSRQs, with the remainder being BL Lac objects and lower luminosity AGN. A similar argument can be made based on the γ -ray spectral index. The median index for FSRQs is $\Gamma = 2.44$ while only 9% of our BL Lac objects have such soft spectra. There are 4 such soft sources in our set of 17 radio sources. Conservatively assuming that all are FSRQs, we infer that twice this number, namely 8, FSRQ are in the radio-detected sample. Of the 29 sources without radio counterparts, 4 are Blazar ‘ANTI-Associations’ (see Abdo et al. 2009, 2010f, for details), where we can definitively exclude any flat-spectrum radio source bright

enough for a *Fermi*-type blazar. While most of these 29 sources lack the very deep radio observations to make an ANTI-Association, all but 5 have been classified as pulsar candidates, based on gamma-ray spectral curvature and lack of variability. We thus suspect that virtually all of these sources are other classes of gamma-ray emitters, eg. pulsars yet to be discovered, starburst galaxies, etc. Our conclusion is that the *likely* incompleteness is only $8/(186+8) = 4\%$. Conservatively adding a few nominally radio-quiet sources from erroneous LAT localizations may allow 5% incompleteness. This correction has been applied in § 4.1 and § 4.2.

Moreover, we show that our results are robust even in the unlikely case that half of the unassociated sources are FSRQs (thus neglecting that the unassociated FSRQs occupy a definite part of the parameter space). In this scenario, the number of *likely* yet unidentified FSRQs is ~ 22 (i.e. $8 + 29/2$). We assign a random redshift, drawn from a smoothed version of the FSRQ redshift distribution to 22 out of the 46 unassociated objects (i.e. giving 10 % maximum incompleteness for the FSRQ sample). These are then used with the associated FSRQs to derive the luminosity function. One example is reported in Table 3. It is apparent that including the unassociated sources with random redshifts does not modify the shape and the parameters of the LF. Indeed, all the parameters are well within the statistical uncertainties of the parameters of the LF derived using only the associated data set. This test shows that the systematic uncertainty introduced by the incompleteness is smaller than the statistical uncertainty. In Appendix A we present a more detailed discussion of other sources of uncertainty.

4.4. Comparison with Previous Results

4.4.1. The Local Luminosity Function

The local LF is the luminosity function at redshift zero. For an evolving population, the local LF is obtained by de-evolving the luminosities (or the densities) according to the best-fit model. This is generally done using the $1/V_{\text{MAX}}$ method of Schmidt (1968), as reported for example by Della Ceca et al. (2008). However, since the best representation of the LF is the LDDE model, the maximum volume has to be weighted by the density evolution relative to the luminosity of the source. In this case, the maximum allowed volume for a given source is defined as:

$$V_{\text{MAX}} = \int_{z_{\text{min}}}^{z_{\text{max}}} \Omega(L_i, z) \frac{e(z, L_i)}{e(z_{\text{min}}, L_i)} \frac{dV}{dz} dz \quad (17)$$

where L_i is the source luminosity, $\Omega(L_i, z)$ is the sky coverage, z_{max} is the redshift above which the source drops out of the survey, and $e(z, L_i)$ is the evolution term of Eq. 15 normalized

(through $e(z_{min}, L_i)$) at the redshift z_{min} to which the LF is to be de-evolved. The LF de-evolved at z_{min} ($z_{min}=0$ in this case) is built using the standard $1/V_{MAX}$ method (Schmidt 1968).

In order to gauge the uncertainties that the different methods might introduce in the determination of the local LF we consider also an alternate method. We perform a Monte Carlo simulation, drawing 1000 series of parameters from the covariance matrix of the best fit LDDE model described in § 4.2. Using the covariance matrix ensures that parameters are drawn correctly, taking into account their correlations. The re-sampled parameters are used to compute the $\pm 1\sigma$ error of the LF at redshift zero. This is reported in Fig. 5. There is very good agreement with the local LFs using this method and the $1/V_{MAX}$ approach. The gray band in Fig. 5 shows the true statistical uncertainty on the space density that the $1/V_{MAX}$ method (applied using the best-fit parameters) is not able to capture.

We find a local LF described by a power law with index of 1.6–1.7, for $F_{100} < 10^{47}$ erg s⁻¹, steepening at higher luminosity. Thus the local LF can be parametrized as a double power law:

$$\Phi(L_\gamma) = \frac{dN}{dL_\gamma} = A \left[\left(\frac{L_\gamma}{L_*} \right)^{\gamma_1} + \left(\frac{L_\gamma}{L_*} \right)^{\gamma_2} \right]^{-1} \quad (18)$$

where $A = (3.99 \pm 0.30) \times 10^{-11}$, $L_* = 0.22 \pm 0.30$, $\gamma_1 = 1.68 \pm 0.17$, $\gamma_2 = 3.15 \pm 0.63$ and both L_γ and L_* are in units of 10^{48} erg s⁻¹. Other models (e.g. a Schechter function, a simple power law etc.) do not generally provide as good a fit to the data. The values of the low-luminosity index γ_1 and the high-luminosity index γ_2 are in good agreement with that found here of 1.63 ± 0.16 and 2.3 ± 0.3 reported by Padovani et al. (2007) for the DRBXS survey of FSRQs.

Values very similar to those found here were also reported for a radio FSRQ sample by Dunlop & Peacock (1990), who find³ $\gamma_1 = 1.83$ and $\gamma_2 = 2.96$. The *Fermi* LF low-luminosity index (i.e. γ_1) is flatter than that determined using EGRET blazars by Narumoto & Totani (2006) as is apparent in Fig. 5. However, a re-analysis of the same data sets employing the blazar sequence (Fossati et al. 1998) to model the blazar SEDs found a low-luminosity index in the 1.8–2.1 range (Inoue & Totani 2009). Also, in a more recent work, Inoue et al. (2010) modified their SED models to be able to reproduce TeV data of known blazars. Their LF at redshift zero (see Fig. 5) is found to be in relatively good agreement with that found here for the *Fermi* sample.

³Their definition of local luminosity function and Eq. 18 differ by a $1/L_\gamma$ (or $1/P$ in their paper) term. Thus we added 1.0 to their exponents.

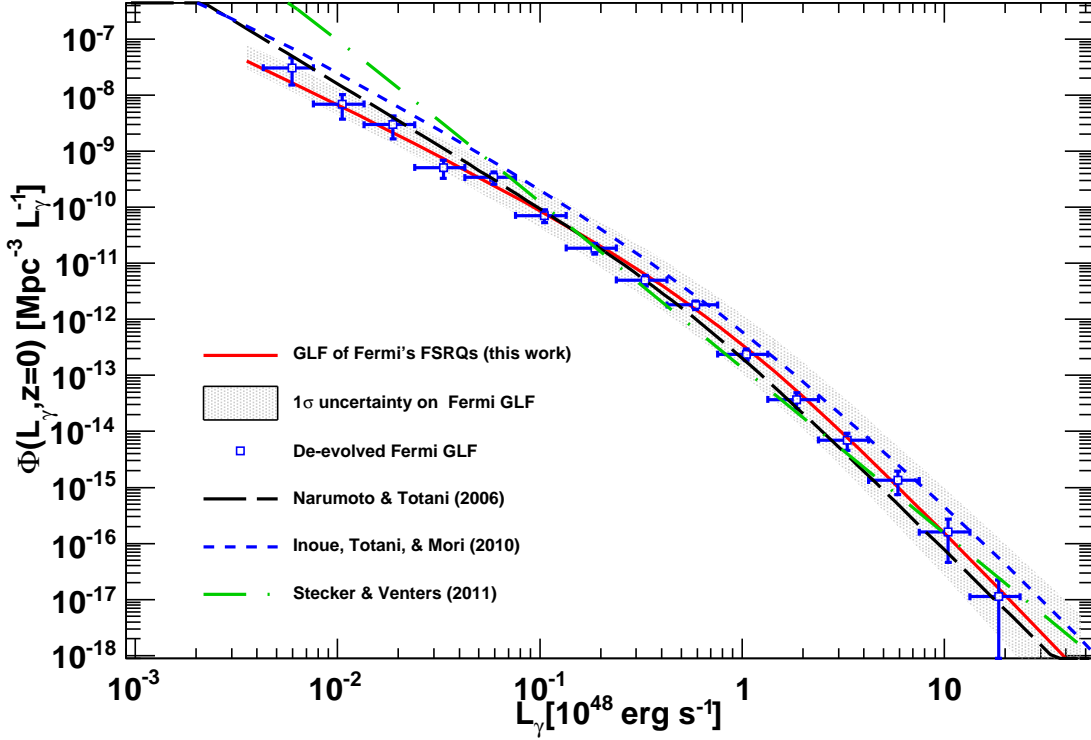


Fig. 5.— Local ($z=0$) LF of the *Fermi* FSRQs as derived from the best-fit LDDE model in § 4.2 (solid line). The gray band represents the $\pm 1\sigma$ uncertainty computed as described in the text. The long- and short-dashed lines show the LF models based on the EGRET blazars derived by Narumoto & Totani (2006) and Inoue et al. (2010) respectively. The dashed-dotted line shows the prediction from the model of Stecker & Venters (2010).

4.4.2. The Luminosity Function at Redshift 1

Fig. 6 shows the luminosity of FSRQ at redshift 1 compared to predictions from recent models. It is apparent that the evolution of the *Fermi* LF is stronger than predicted by any of these models. The increase in space density from redshift 0 to 1 for a source with a luminosity of $10^{48} \text{ erg s}^{-1}$ is almost a factor ~ 150 . This dramatic increase is not seen in the evolution of radio-quiet AGN (e.g. Ueda et al. 2003; Hasinger et al. 2005) whose space density increases by a factor 25–50 between redshift 0 and 1. The increase of a factor ~ 60 seen in FSRQs detected in Radio Dunlop & Peacock (1990), is still slower than that of *Fermi* blazars. This explains why the predictions based on luminosity functions derived at other wavelengths (see Fig. 6) underpredict the density of high-luminosity *Fermi* FSRQs at redshift of 1.

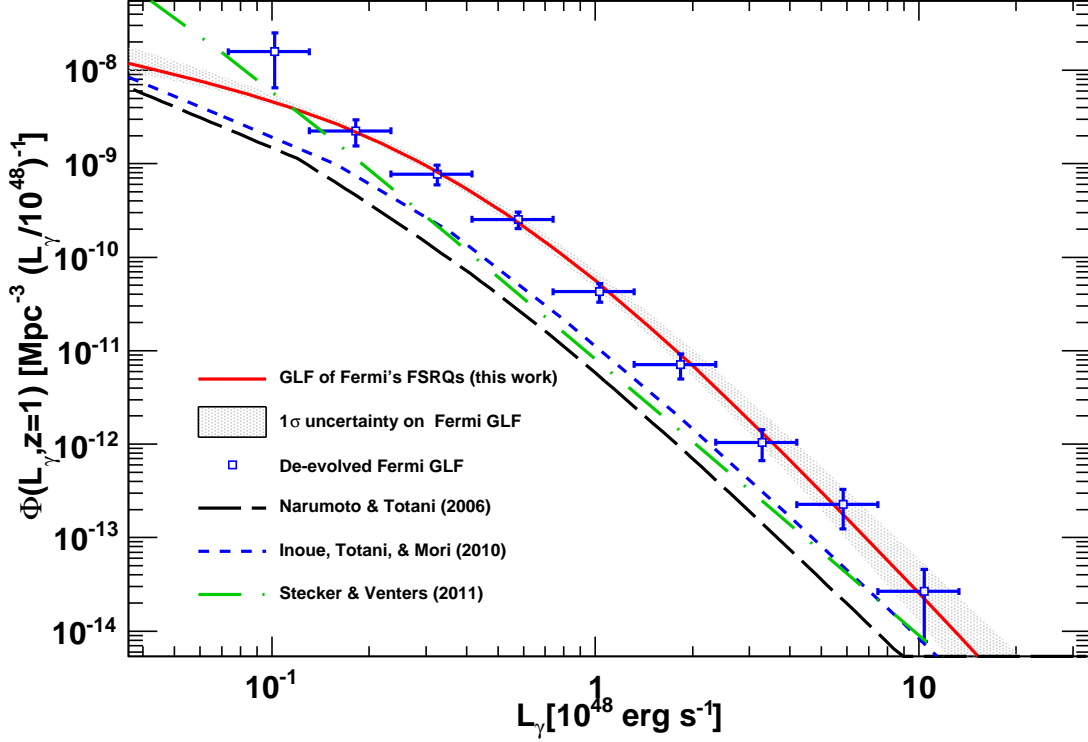


Fig. 6.— LF of the *Fermi* FSRQs at redshift 1.0 as derived from the best-fit LDDE model in § 4.2 (solid line). The gray band represents the $\pm 1\sigma$ uncertainty computed with the method described in the text. The long dashed and short dashed lines show the LF models based on the EGRET blazars derived respectively by Narumoto & Totani (2006) and Inoue et al. (2010). The dashed-dotted line shows the prediction from the model of Stecker & Venters (2010).

5. The Spectral Energy Distributions of FSRQs

We may use the 0.1–300 GeV LAT spectra of our uniform bright *Fermi* FSRQ sample along with the 15–200 keV spectra measured by the *Swift*-BAT to characterize the high energy Inverse Compton (IC) sector of the blazar SED. In turn this allows us to describe the average SED properties of the energetic blazars and to estimate their contribution to the cosmic high-energy backgrounds.

5.1. Data Analysis

For this analysis, we further restrict the sample to $F_{100} \geq 7 \times 10^{-8} \text{ ph cm}^{-2} \text{ s}^{-1}$ (corresponding to an energy flux of $3.4 \times 10^{-11} \text{ erg s}^{-1} \text{ cm}^{-2}$ for a power law with an index of 2.45), since for brighter sources *Fermi* has a negligible bias in the detected spectral indices and FSRQs are selected uniformly (Abdo et al. 2010e). For fainter sources hard-spectrum objects (principally BL Lac objects) dominate the sample. There are 103 bright FSRQs detected by *Fermi* that meet these criteria (Abdo et al. 2010f).

We analyze two years of *Fermi* data using version V9r21 of the science tools⁴. The data are filtered, removing time periods in which the instrument was not in sky-survey mode and photons whose zenith angle is larger than 100 degrees. We consider only photons collected within 15 degrees of the source position with $100 \text{ MeV} \leq E \leq 300 \text{ GeV}$. We employ the P7SOURCE_V6 instrumental response function (IRF) and perform binned likelihood analysis using the *gtlike* tool. First, a likelihood fit using a power-law model for all the sources in the region of interest (ROI) is performed on the entire energy band (100 MeV–300 GeV). The parameters (i.e. flux and photon index) of all the sources within 3° of the target FSRQ, along with the normalization of the diffuse model, are left free. More distant sources have parameters frozen at the 2FGL measured values (Abdo 2011). We next choose 30 logarithmically spaced energy bins and perform a binned likelihood in each, deriving the flux of the target FSRQ in each energy bin. During this exercise the flux of the FSRQ is allowed to vary while the photon index is fixed at the best-fit value found for the whole band. All the neighboring sources had parameters fixed at the best-fit values, although the diffuse emission normalization was allowed to vary. This analysis provides a 30-bin 100 MeV–300 GeV energy spectrum for all 103 sources in the bright FSRQ sample.

Swift-BAT is a coded-mask telescope that has conducted a several year survey in the 15–200 keV hard X-ray sky (Gehrels et al. 2004; Barthelmy et al. 2005). With this deep exposure, BAT reaches a sensitivity of $\sim 10^{-11} \text{ erg cm}^{-2} \text{ s}^{-1}$ on most of the high-latitude sky (e.g. Tueller et al. 2007; Ajello et al. 2008a,c; Cusumano et al. 2010). Blazars represent 15–20 % of the extragalactic source population detected by BAT (Ajello et al. 2009b). Since *Fermi*-LAT and *Swift*-BAT have comparable sensitivity in their respective bands⁵ and since the two bands cover the bulk of the IC component, a joint study allows an accurate characterization of the IC spectrum and the contribution to the background.

⁴<http://fermi.gsfc.nasa.gov/ssc/data/analysis/software/>

⁵A *Fermi* FSRQ with a photon flux of $3 \times 10^{-8} \text{ ph cm}^{-2} \text{ s}^{-1}$ in the 100 MeV–100 GeV band and a power-law spectrum with an index of 2.4 has a energy flux of $1.5 \times 10^{-11} \text{ erg cm}^{-2} \text{ s}^{-1}$.

We use ~ 6 years of BAT data to extract a 15–200 keV spectrum for all the FSRQs in the *Fermi* sample. Spectral extraction is performed according to the recipes presented by Ajello et al. (2008c) and discussed in detail by Ajello et al. (2009a) and Ajello et al. (2010). Both BAT and LAT spectra are multiplied by $4\pi D_L(z)^2$ (with $D_L(z)$ the luminosity distance at redshift z) to transform the flux into a luminosity and shifted by $(1+z)$ to transform into source rest-frame SEDs.

For each FSRQ, we fit the BAT and LAT data with an empirical model of the following form:

$$E^2 \frac{dN}{dE} \cdot 4\pi D_L(z)^2 = E^2 \left[\left(\frac{E}{E_b} \right)^{\gamma_{BAT}} + \left(\frac{E}{E_b} \right)^{\gamma_{LAT}} \right]^{-1} \cdot e^{-\sqrt{E/E_c}} \cdot 4\pi D_L(z)^2 \quad (19)$$

where γ_{BAT} and γ_{LAT} are the power-law indices in the BAT and the LAT bands and E_b and E_c are the break and the cut-off energy, respectively. The $e^{-\sqrt{E/E_c}}$ term allows us to model the curvature that is clearly visible in a few of the *Fermi* spectra. The fit is performed only for $E < 20$ GeV to avoid possible steeping due to the absorption of γ -ray photons by the extra-galactic background light (EBL; e.g. Stecker et al. 2006; Franceschini et al. 2008).

Two sample spectra are shown in Fig. 7. It is apparent that for the brightest FSRQs, BAT and LAT are efficient in constraining the shape of the IC emission. Even when the BAT signal is not significant, the upper limit from BAT still provides useful constraints on the low energy curvature of the SED. In a number of bright sources (see e.g. Fig. 7) the highest-energy datapoint in BAT at ≥ 120 keV is seen to deviate from the baseline fit. This deviation is at present not significant (i.e. the reduced χ^2 of the baseline fit is already ≈ 1.0), but certainly suggestive of a second component. Observations with INTEGRAL extending to energies ≥ 200 keV might ascertain the nature of this feature.

Several caveats necessarily apply to our analysis. First, the BAT and LAT observations are not strictly simultaneous. LAT spectra are accumulated over 2 years while the BAT data span 6 years. In principle one could restrict the BAT data to the period spanned by the *Fermi* observations. In practice this would seriously limit the BAT sensitivity, weakening constraints on most of the spectra. Second, it is possible that BAT and LAT are not sampling exactly the same emission component. In particular, BAT might be dominated by IC emission produced by the synchrotron self Compton (SSC, Maraschi et al. 1992) component while the LAT may be more sensitive to External Compton (EC, Dermer & Schlickeiser 1993) emission. Ultimately detailed SED modeling with strictly simultaneous data would be needed to eliminate these concerns, and such work is well beyond the scope of this paper. Bearing these caveats in mind, our bright sample is nearly free of selection effects other than the hard flux-limit threshold applied to the *Fermi* data. This allows an detailed study of the average properties of the high-energy SED of FSRQs.

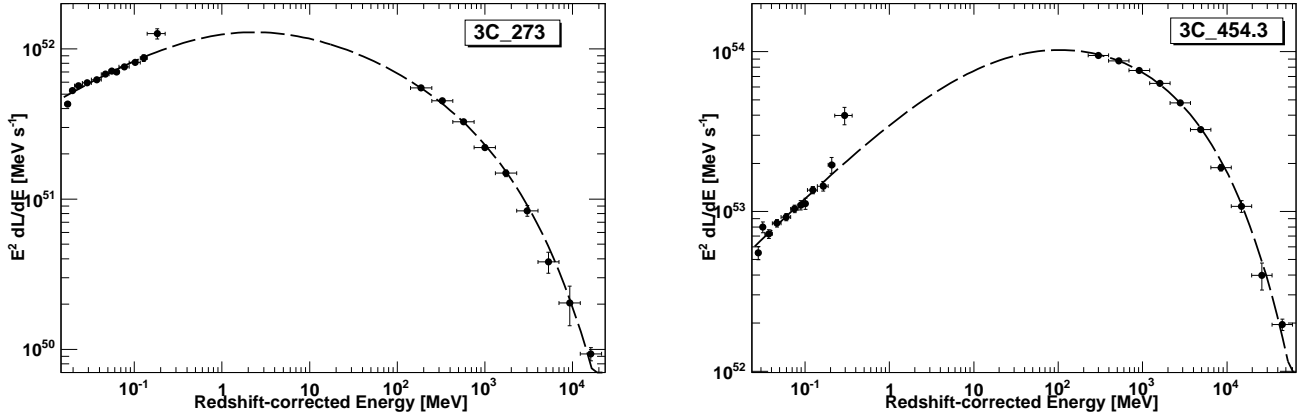


Fig. 7.— Two BAT–LAT spectra of famous blazars fitted with the empirical model described in § 5.

5.2. Correlation of Peak Luminosity and the Energy of the Peak

We can compare the Inverse Compton rest-frame peak luminosity and peak energy from the SED fits to the FSRQ in our sample. As shown in Figure 8, there is no apparent correlation between these quantities; indeed the Kendall test gives a value $\tau = 0.09$ indicating no significant correlation. Since generally neither *Fermi* nor BAT directly sample the high-energy peak, we also fit the spectra using a third degree polynomial function instead of the model in Eq. 19. The results are shown in the right panel of Fig. 8 and confirm the previous findings.

This is in contrast to the correlation found (but see also Nieppola et al. 2008) between the luminosity and the energy of the *synchrotron* peak of blazars (e.g. Ghisellini et al. 1998; Fossati et al. 1998). This might imply that the jet parameters (e.g. Doppler factor, luminosity of the target photon field, etc.) do not depend on blazar GeV luminosity or redshift. This may be understood if the IC peak is largely controlled by EC emission for these sources.

5.3. Average SEDs

It is useful to estimate the average SED of FSRQs, particularly for estimating the contribution of FSRQs to the extragalactic gamma-ray background. First we define the

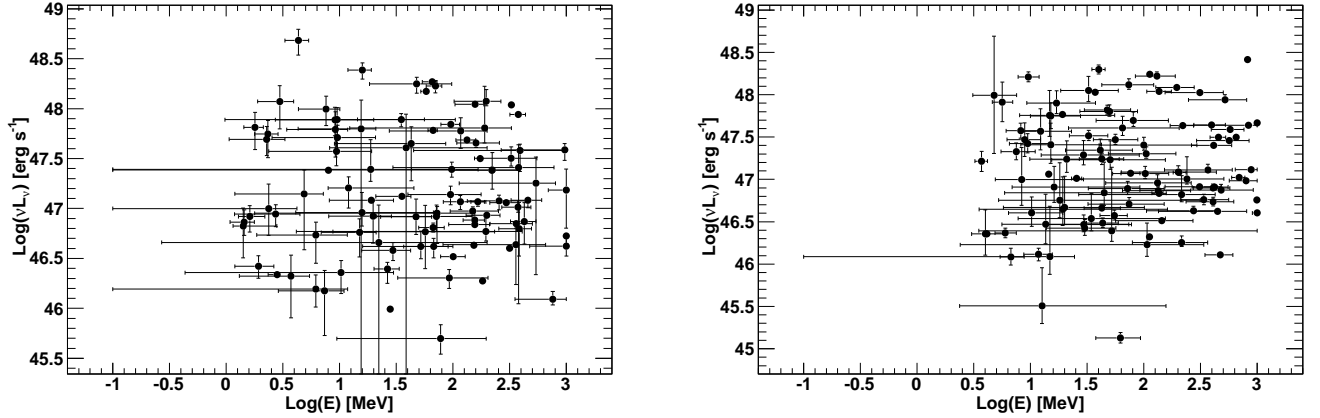


Fig. 8.— Peak luminosity versus the energy of the peak for the complete sample of FSRQs discussed in § 5. The left plot shows the value derived using a double power law with exponential cut-off while the right panel show parameters derived using a third degree polynomial function.

bolometric luminosity as the luminosity in the 10 keV – 300 GeV band⁶ and divide the sources into four bins of bolometric luminosity with approximately the same number of objects in each bin. In these luminosity bins we compute the average of the logarithm of the spectral luminosity at each energy. Associated errors on this average spectrum are computed using the Jackknife technique. In this framework we neglect uncertainties due to different level of the energy density of the extragalactic background light which would affect mostly the high-energy part of the SED (i.e. ≥ 20 GeV).

Fig. 9 shows the average rest-frame SED for the FSRQ sample in the four luminosity bins. This plot confirms the lack of a systematic correlation of the peak luminosity and energy. Indeed, all the averaged SEDs show a peak in the 10–100 MeV band and their shape does not change much with luminosity.

To transform luminosities between observed and rest-frame we need the k-correction, along with its redshift variation, shown in Fig. 10. In practice, there is little difference between the k-correction for the average SED computed here (even applying EBL absorption, e.g. Franceschini et al. 2008) and one computed for a power law (i.e. $(1+z)^{\Gamma-2}$) with a photon index of 2.4. Only at large redshifts do the two k-corrections start to differ; this difference is only $\sim 5\%$ at a redshift of 4. We find that using a power law index of 2.37 and taking into

⁶The best fit is extrapolated from 20 GeV to 300 GeV.

account EBL absorption allows us to reproduce correctly the k-correction up to redshift ~ 6 .

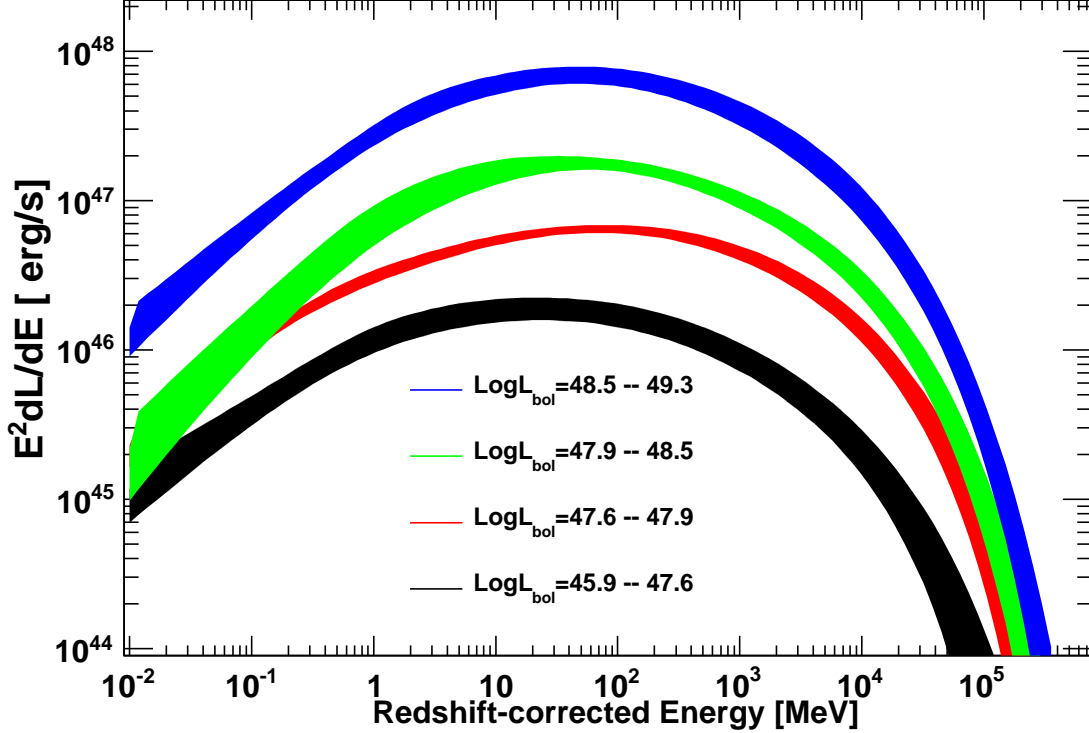


Fig. 9.— Average rest-frame spectral energy distributions for four representative FSRQ luminosity classes (left panel), see § 5.3. In each SED, the band represents the 1σ uncertainty on the average. This does not reflect the uncertainty connected to the level of the extragalactic background light.

6. The Contribution to the Isotropic Gamma-Ray Background

The nature of the diffuse gamma-ray background at GeV energies remains one of the most interesting problems in astrophysics. The presence of an isotropic component was first determined by the OSO-3 satellite (Kraushaar et al. 1972) and confirmed by SAS-2 and EGRET (respectively Fichtel et al. 1975; Sreekumar et al. 1998). This isotropic component is normally referred to as the isotropic gamma-ray background (IGRB). *Fermi* recently provided a refined measurement of this isotropic component showing that it can be adequately described as a single power law with an index of 2.4 in the 200 MeV – 100 GeV energy range

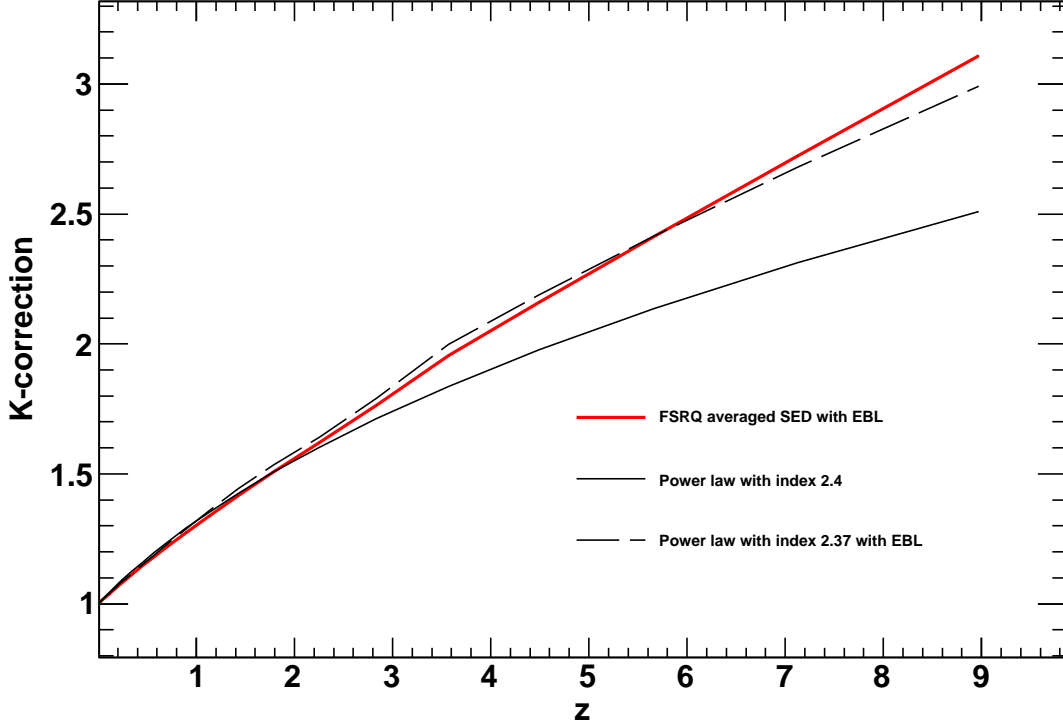


Fig. 10.— Ratio of source rest-frame luminosity to observed luminosity (i.e. k-correction) as a function of redshift for the average SED shape reported in § 5.3 and for two generic power laws.

(Abdo et al. 2010d).

Blazars, representing the most numerous identified populations by EGRET and *Fermi* extragalactic skies, are expected to produce a substantial fraction of the IGRB. Typical predictions range from 20–30 % (Chiang & Mukherjee 1998; Mücke & Pohl 2000; Narumoto & Totani 2006; Dermer 2007; Inoue & Totani 2009) to 100 % (Stecker & Salamon 1996; Stecker & Venters 2010). Analysis of the source-count distribution showed that for $F_{100} \geq 10^{-9} \text{ ph cm}^{-2} \text{ s}^{-1}$ the contribution of *unresolved* blazars to the IGRB is $\sim 16\%$ in the 100 MeV – 100 GeV band (Abdo et al. 2010e). Since the source counts distribution show a strong break at a flux of $F_{100} \approx 6 \times 10^{-8} \text{ ph cm}^{-2} \text{ s}^{-1}$, it was concluded that extrapolating the source counts to zero flux would produce $\sim 23\%$ of the IGRB.

Now, with a measured LF we can more robustly evaluate the emission arising from faint FSRQs. In addition, the FSRQ SED shape study of the previous section also allows

improvement over the simple power-law type spectra assumed by Abdo et al. (2010e).

The contribution of ‘unresolved’ FSRQs to the IGRB can be estimated as:

$$F_{EGB} = \int_{z_{min}}^{z_{max}} dz \frac{dV}{dz} \int_{\Gamma_{min}}^{\Gamma_{max}} d\Gamma \int_{L_{\gamma,min}}^{L_{\gamma,max}} dL_{\gamma} F_{\gamma}(L_{\gamma}, z) \frac{d^3 N}{dL_{\gamma} dz d\Gamma} \left(1 - \frac{\Omega(\Gamma, F_{\gamma})}{\Omega_{max}} \right) \quad (20)$$

where the limit of integration are the same as those of Eq. 5 and $F_{\gamma}(L_{\gamma}, z)$ is the flux of a source with rest-frame luminosity L_{γ} at redshift z . Since we are interested in the diffuse flux not yet resolved by *Fermi* (Abdo et al. 2010d) the term $(1 - \Omega(\Gamma, F_{\gamma})/\Omega_{max})$ takes into account the photon index and source flux dependence of the LAT source detection threshold (see Abdo et al. 2010e, for more details). The limits of integration of Eq. 20 are the same as those of Eq. 5.

In Eq. 20 setting $\Omega(\Gamma, F_{\gamma})/\Omega_{max}=0$ allows us to compute the total γ -ray emission arising from the FSRQ class. The result is $3.13_{-0.25}^{+0.37} \times 10^{-6}$ ph cm⁻² s⁻¹ sr⁻¹ in the 100 MeV – 100 GeV band. This value should be compared with the total sky intensity of 1.44×10^{-5} ph cm⁻² s⁻¹ sr⁻¹, which includes IGRB plus detected sources (Abdo et al. 2010d). Thus FSRQs make $21.7_{-1.7}^{+2.5}$ % of this total intensity.

If one considers the contribution only from the FSRQs that *Fermi* has not detected then this becomes $9.66_{-1.09}^{+1.67} \times 10^{-7}$ ph cm⁻² s⁻¹ sr⁻¹ (with a maximum systematic uncertainty of 3×10^{-7} ph cm⁻² s⁻¹ sr⁻¹ see § A). This represents $9.3_{-1.0}^{+1.6}$ % of the IGRB intensity in the 0.1–100 GeV band (Abdo et al. 2010d). From above it is also clear that *Fermi* has already resolved more than 50 % of the total flux arising from the FSRQ class. Fig. 11 shows this contribution. The possible presence of external Compton components in the SEDs of FSRQs makes the estimate between 200 keV and 100 MeV uncertain (see § 5.3). Future observations with both *Fermi* above 20 MeV and INTEGRAL above 200 keV and physical modeling of blazar spectra might substantially reduce this uncertainty.

Even the (disfavored) PLE model cannot accommodate a much larger contribution of FSRQs to the IGRB. Indeed, in this case the contribution of *unresolved* FSRQs would be 1.37×10^{-6} ph cm⁻² s⁻¹ sr⁻¹ (or ~ 13 % of the IGRB intensity).

7. Beaming: The Intrinsic Luminosity Function and the Parent Population

The luminosities L defined in this work are apparent isotropic luminosities. Since the jet material is moving at relativistic speed ($\gamma > 1$), the observed, Doppler boosted, luminosities are related to the intrinsic values by:

$$L = \delta^p \mathcal{L} \quad (21)$$

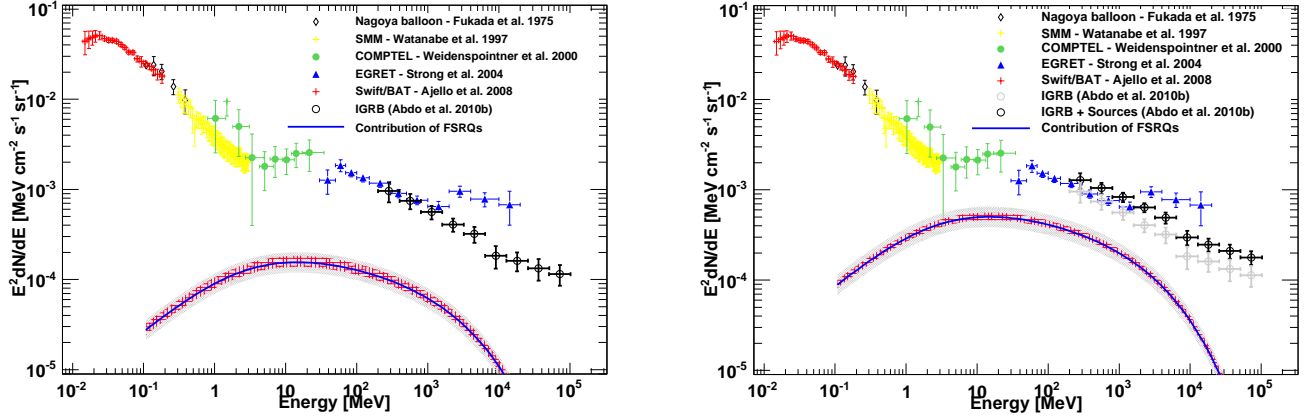


Fig. 11.— Contribution of *unresolved* (left) and all (right) FSRQs to the diffuse extragalactic background (blue line) as determined by integrating the luminosity function coupled to the SED model derived in § 5.3. The hatched band around the best-fit prediction shows the 1σ statistical uncertainty while the gray band represents the systematic uncertainty.

where \mathcal{L} is the intrinsic (unbeamed) luminosity and δ is the kinematic Doppler factor

$$\delta = \left(\gamma - \sqrt{\gamma^2 - 1} \cos \theta \right)^{-1} \quad (22)$$

where $\gamma = (1 - \beta^2)^{-1/2}$ is the Lorentz factor and $\beta = v/c$ is the velocity of the emitting plasma. Assuming that the sources have a Lorentz factor γ in the $\gamma_1 \leq \gamma \leq \gamma_2$ range then the minimum Doppler factor is $\delta_{min} = \gamma_2^{-1}$ (when $\theta=90^\circ$) and the maximum is $\delta_{max} = \gamma_2 + \sqrt{\gamma_2^2 - 1}$ (when $\theta = 0^\circ$). We adopt a value of $p = 4$ that applies to the case of continuous jet emission which seems appropriate for the study presented here since long-term average luminosities are used. The case $p = 4$ applies also to spherical blobs if the observed emission is dominated by the SSC component, while a value of $p=5-6$ should be adopted if the emission is due to external Compton (Dermer 1995). However, as shown later these values imply extremely small isotropic rest-frame luminosities.

Beaming is known to alter the shape of the intrinsic luminosity function. Urry & Shafer (1984) provide an analytic solution to the case where the intrinsic luminosity function is a single power law and the jets have a single Lorentz factor. In Urry & Padovani (1991) the intrinsic luminosity function may be a double power law and a distribution of Lorentz factor is considered.

In this Section we will determine the intrinsic luminosity function of the *Fermi* FSRQs and their Lorentz and Doppler factor distributions. In what follows we adopt the formalism

and symbols of Lister (2003) and Cara & Lister (2008).

We begin by defining the intrinsic luminosity function as:

$$\Phi(\mathcal{L}) = k_1 \mathcal{L}^{-B} \quad (23)$$

valid in the $\mathcal{L}_1 \leq \mathcal{L} \leq \mathcal{L}_2$ range. The probability of observing a beamed luminosity L given a Doppler factor δ is (see also Lister 2003):

$$P(L, \delta) = P_\delta(\delta) * \Phi(\mathcal{L}) \frac{d\mathcal{L}}{dL} \quad (24)$$

where $P_\delta(\delta)$ is the probability density for the Doppler δ . Assuming a random distribution for the jet angles (i.e. $P_\theta = \sin \theta$), this results in

$$P_\delta(\delta) = \int P_\gamma(\gamma) P_\theta(\theta) \left| \frac{d\theta}{d\delta} \right| d\gamma = \int P_\gamma(\gamma) \frac{1}{\gamma \delta^2 \beta} d\gamma. \quad (25)$$

From here it follows that

$$P_\delta(\delta) = \delta^{-2} \int_{f(\delta)}^{\gamma_2} \frac{P_\gamma(\gamma)}{\sqrt{\gamma^2 - 1}} d\gamma \quad (26)$$

where $P_\gamma(\gamma)$ is the probability density for γ and the lower limit of integration $f(\delta)$ depends on the Doppler factor value and is reported in Eq. A6 in Lister (2003). Integrating over δ yields the observed luminosity function of the Doppler beamed FSRQs:

$$\Phi(L) = k_1 L^{-B} \int_{\delta_1(L)}^{\delta_2(L)} P_\delta(\delta) \delta^{p(B-1)} \quad (27)$$

where, as in Cara & Lister (2008), the limits of integration are

$$\delta_1(L) = \min\{\delta_{max}, \max(\delta_{min}, (L/\mathcal{L}_2)^{1/p})\} \quad (28)$$

$$\delta_2(L) = \max\{\delta_{min}, \min(\delta_{max}, (L/\mathcal{L}_1)^{1/p})\} \quad (29)$$

In this way, by fitting Eq. 27 to the *Fermi* Doppler boosted LF, it is possible to determine the parameters of the intrinsic luminosity function and of the Lorentz-factor distribution.

We assume that the probability density distribution for γ is a power law of the form

$$P_\gamma(\gamma) = C \gamma^k \quad (30)$$

where C is a normalization constant and the function is valid for $\gamma_1 \leq \gamma \leq \gamma_2$. Here we assume $\gamma_1 = 5$ and $\gamma_2 = 40$ as this is the range of Lorentz factors observed for γ -loud blazars (e.g. Lähteenmäki & Valtaoja 2003; Lister et al. 2009a; Savolainen et al. 2010). While the largest intrinsic luminosity (\mathcal{L}_2) can be set free, the lowest one depends on the value of p

chosen: i.e. from Eq. 21 the beaming factor defines the intrinsic luminosity corresponding to the apparent isotropic luminosity we observe. For $p=4$ and $p=5$, \mathcal{L}_1 has to be set $10^{40} \text{ erg s}^{-1}$ and $10^{38} \text{ erg s}^{-1}$ respectively. We set $\mathcal{L}_2 = 10^4 \mathcal{L}_1$, but this choice has hardly any impact on the results.

The free parameters of the problem are: the normalization (k_1) and the slope (B) of the intrinsic LF and the slope k of the Lorentz factor distribution. We have fitted Eq. 27 to the *Fermi* LF de-evolved at redshift zero derived in §4.4.1. Fig. 12 shows how the best-fit beaming model reproduces the local LF of FSRQs measured by *Fermi*. From the best-fit we derive, for the $p = 4$ case, an intrinsic LF slope of $B = 3.04 \pm 0.08$ and an index of the Lorentz-factor distribution of $k_1 = -2.03 \pm 0.70$. The fit values are summarized in Table 4. The Lorentz-factor distribution implies an average Lorentz factor of detected *Fermi* blazars of $\gamma = 11.7^{+3.3}_{-2.2}$, in reasonable agreement with measured values (see e.g. Ghisellini et al. 2009). The index of the Lorentz-factor distribution is in agreement with $k_1 \sim -1.5$ found for the CJ-F survey (Lister & Marscher 1997). The parameters for the $p = 5$ case are very similar to those of the $p = 4$ case, but the reduced χ^2 is slightly worse (see Table 4). Nevertheless, the predictions of the two models are in agreement and we find again that the average bulk Lorentz factor is $\gamma = 10.2^{+4.8}_{-2.4}$. As noted already the extreme Doppler boosting (δ^5) requires the intrinsic luminosities to be small: i.e. $10^{38} \text{ erg s}^{-1} \leq \mathcal{L} \leq 10^{42} \text{ erg s}^{-1}$.

From the ratio of the integrals of the beamed and intrinsic LF we derive that the *Fermi* FSRQs represent only 0.1 % of the parent population. The average space density of LAT FSRQs (derived from the LF § 4.2) is 1.4 Gpc^{-3} , implying that the average space density of the parent population is $\sim 1500 \text{ Gpc}^{-3}$. Our model also allows us to determine the distribution of jet angles with respect to our line of sight. This is found to peak at ~ 1.0 degrees (Fig. 13). While FSRQs can still be detected at large (i.e. ≥ 10 degrees) off-axis angles for reasonably low γ factors ($\sim 5-7$), most FSRQs detected by *Fermi* are seen at angles less than 5 degrees from the jet axis. Owing to their larger space density (see Fig. 12) misaligned jets produce a non-negligible diffuse emission. From our model it is found that the ratio between the diffuse emission contribution of misaligned jets and that of blazars (at redshift zero) is ~ 30 %. This has obvious consequences for the generation of the IGRB. In fact nearly all of the flux produced by radio galaxies is unresolved, with only 2 steep-spectrum radio quasars, and 2 FR II and 7 FR I radio galaxies detected with the *Fermi* LAT (Abdo et al. 2010b). All the results reported above apply to both the $p = 4$ and $p = 5$ models.

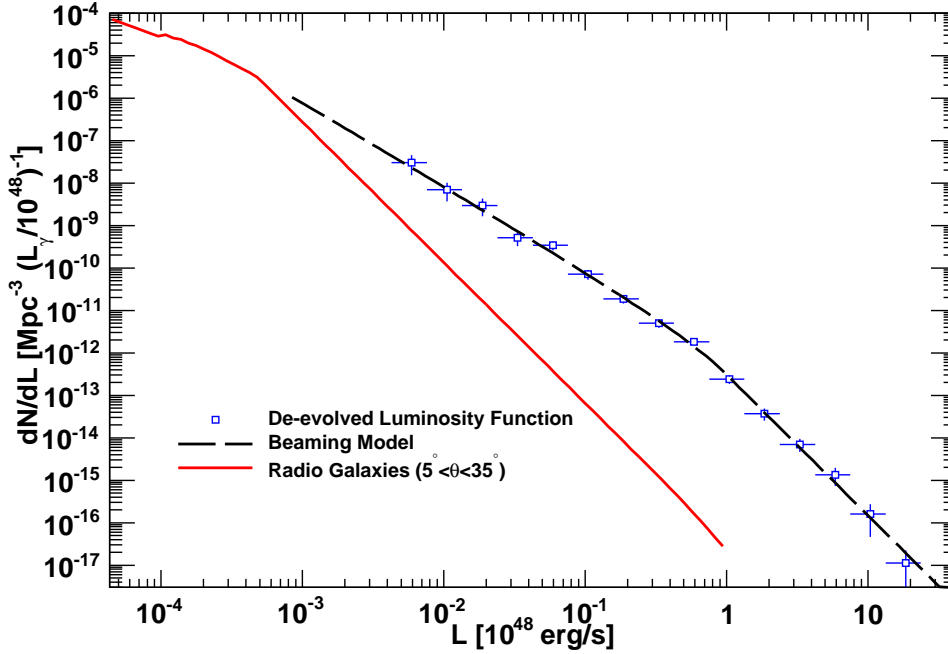


Fig. 12.— *Fermi*’s LF de-evolved at redshift zero and the best-fit beaming model (for $p=4$, see text) described in § 7. The red continuous line shows the predicted space density of misaligned jets.

8. Discussion and Conclusions

In this paper we examine the properties of γ -ray selected FSRQs using data from the *Fermi*-LAT instrument. Our work relies on a nearly complete, flux-limited sample of 186 FSRQs detected by *Fermi* at high significance and large Galactic latitude during the first year of operations. This analysis explores several of the properties of FSRQs; here we discuss and summarize our findings.

8.1. Beamed Luminosity Function

The redshift-zero LF of *Fermi* FSRQs is well described by a double power-law model, typical for the LF of AGN (both of the radio-quiet and radio-loud). At mid-to-high luminosities there is good agreement between the *Fermi* LF and that determined using EGRET data (e.g. Narumoto & Totani 2006; Inoue et al. 2010). At luminosities $\leq 10^{46} \text{ erg s}^{-1}$ the FSRQ LF appears to be slightly flatter than in previous studies.

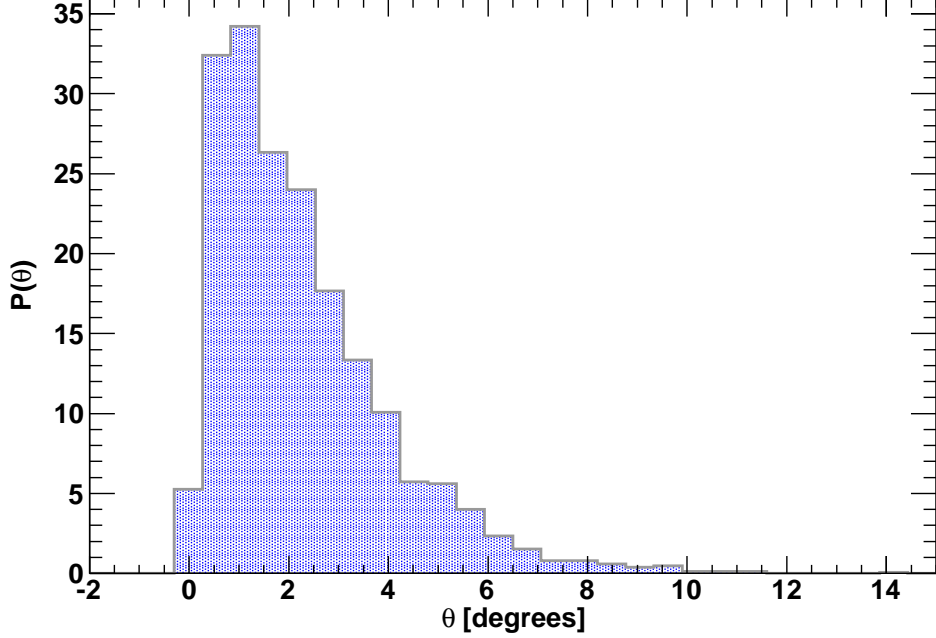


Fig. 13.— Distribution of viewing angles with respect to the jet axis for *Fermi* FSRQs.

The space density of LAT-detected FSRQs increases dramatically with redshift, growing by 50–100 \times by $z=1.5$. Describing the evolution of the LF as simple luminosity evolution (PLE model), there are strong indications that the evolution must cut off for $z \geq 1.6$. After this redshift, the space density of blazars starts to decrease quickly.

A simple PLE does not fully explain the *Fermi* data. In particular the source count distribution is not well modeled. Since there is evidence that low- and high-luminosity sources have different redshift peaks, we consider a more sophisticated model where the evolution is primarily in density, but objects with different luminosity are allowed to have different redshift peaks. This so-called LDDE model explains well the evolutionary behavior of (radio-quiet) AGN selected in the X-ray band (Ueda et al. 2003; Hasinger et al. 2005) and was also suggested by Narumoto & Totani (2006) to describe the LF of EGRET blazars. The LDDE model provides a good description of the LF of the *Fermi* FSRQs. We find that the predictions reported in the literature (e.g. Narumoto & Totani 2006; Inoue et al. 2010; Stecker & Venters 2010) are not in agreement with the LF of *Fermi* FSRQs at redshift unity. This is due to the fact that the *Fermi* FSRQs is found to evolve more quickly than the LFs of X-ray-selected AGN or radio-selected FSRQs. Indeed, the space density of *Fermi* FSRQs increases by a factor ~ 150 between redshift 0 and 1 while the density increase is at most a

factor ~ 60 for the models discussed above.

The LDDE model implies that sources with a luminosity of $10^{46} \text{ erg s}^{-1}$, $10^{47} \text{ erg s}^{-1}$, and $10^{48} \text{ erg s}^{-1}$ reach their maximum space density at a redshift of ~ 0.6 , ~ 0.9 , and ~ 1.5 respectively. It is clear, then, that the most luminous objects, while lower in numbers, appear before the bulk of the (low-luminosity) population. This is the first time that this is seen in γ -rays. This “anti-hierarchical” behavior, where the largest structures come first is common to all classes of AGN (see e.g. Cowie et al. 1999; Hasinger et al. 2005, and references therein), and is often referred to as “cosmological downsizing”. The disappearance of quasar-like objects at late times might indicate that accretion efficiency evolves as a function of cosmic time (e.g. Merloni 2004). Di Matteo et al. (2005) (but see also Sanders et al. 1988) propose that the merging of two massive galaxies leads to, in addition to strong star formation activity, a burst of inflow feeding gas to the SMBH and initiates a ‘quasar-like’ phase. Eventually the energy released by the AGN in the form of powerful winds expels the gas, quenches star formation and starves the AGN. This picture, coupled with the fact that major mergers become increasingly rare at low redshift (e.g. Fakhouri et al. 2010; Kulkarni & Loeb 2011) may explain why quasars are rare in the local Universe.

Fig. 14 shows the energy density injected in the Universe (e.g. the luminosity density) by FSRQs as function of redshift. This shows a broad peak between a redshift of 1 and 2. A similar behavior is shown by the cosmic star-formation history (e.g. Hopkins & Beacom 2006) which peaks around redshift 1-2. This represents a strong link between the host and the nucleus. A noteworthy fact is the mild evidence for a fast decline in the space density of FSRQs after the redshift peak (see parameter p_2 in Table 3). The decline seems to be as dramatic as the increase in space density leading up to the redshift peak. For comparison, X-ray selected samples of AGN show a much milder decline ($p_2 \approx -1.5$) after the redshift peak (e.g. Ueda et al. 2003; Hasinger et al. 2005; Aird et al. 2010). However, recently Silverman et al. (2008) (but see also Schmidt et al. 1995) reported evidence for a similarly dramatic decrease in the space density of AGN.

One factor contributing to this phenomenon is the difficulty for *Fermi* to detect soft sources (Abdo et al. 2010e). At redshift ≥ 3 the SED peak should move well below the current LAT energy band, making it difficult to probe a population of extremely soft sources. Increasing the effective area at or below 100 MeV may help uncover such a population. Because the rising part of the IC peak is in the hard ($\geq 10 \text{ keV}$) X-ray band, high-redshift objects are more easily selected in this band (see e.g. the *Swift*/BAT results in Ajello et al. (2009b)). In this case another strategy would be to build a bolometric luminosity function that uses both the γ -ray and the X-ray selected samples.

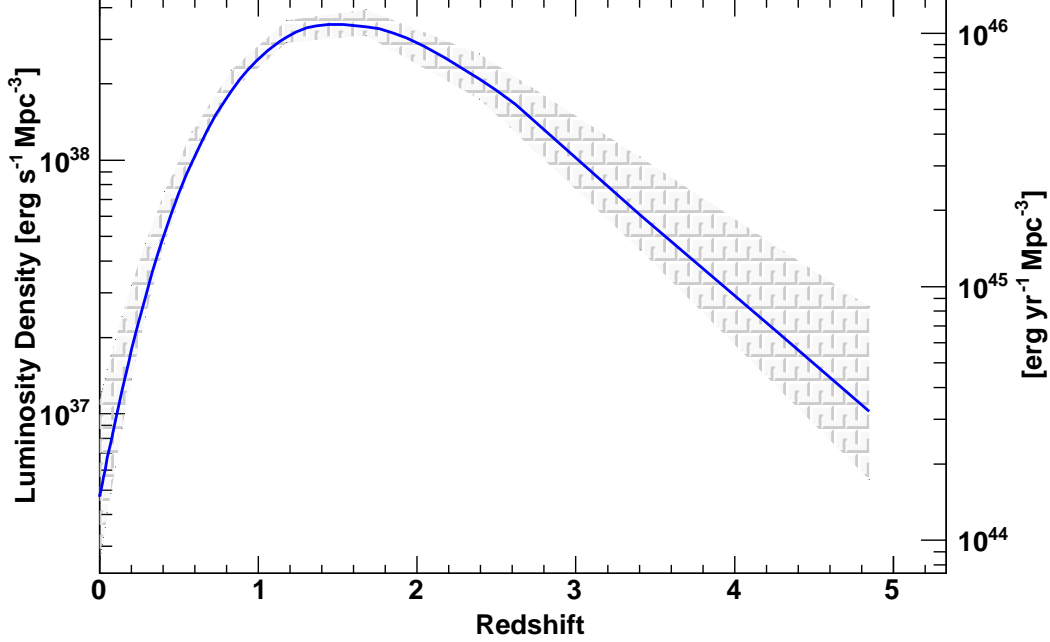


Fig. 14.— Luminosity density as a function of redshift produced by the *Fermi* FSRQs. The gray band represents the 1σ statistical uncertainty around the best-fit LF model.

8.2. The Intrinsic Luminosity Function

Doppler boosting allows *Fermi* to detect many blazars when their jet emission is within a few degrees from the line of sight. As shown first by Urry & Shafer (1984), Doppler boosting is known to alter the shape of the luminosity function. In this paper, we adopted a formalism that allowed us to recover the intrinsic de-beamed LF and to determine the distribution of bulk Lorentz factors for the *Fermi* FSRQs.

The intrinsic LF is compatible with a single steep power law with an index of 3.04 ± 0.08 in the range of intrinsic luminosities $10^{40} \text{ erg s}^{-1} \leq \mathcal{L} \leq 10^{44} \text{ erg s}^{-1}$. The break seen in the *beamed* LF at redshift zero is thus produced by Doppler boosting. The data cannot be explain by a single, averaged, Lorentz factor, but require a distribution of Lorentz factors. This distribution is found to be compatible with a power law with an index of -2.03 ± 0.70 in the $5 \leq \gamma \leq 40$ range. This yields the result that the average FSRQ bulk Lorentz factor is $\Gamma = 11.7_{-2.2}^{+3.3}$, in good agreement with several studies (Ghisellini et al. 2009). Our model is able to predict the distribution of viewing angles with respect to the jet axes of *Fermi* FSRQs. It is found, see Fig. 13, that on average FSRQs are seen within an average angle of $\sim 2.3^\circ$ from the jet and that most are seen within 5° - 6° . A few *Fermi* FSRQ detections may

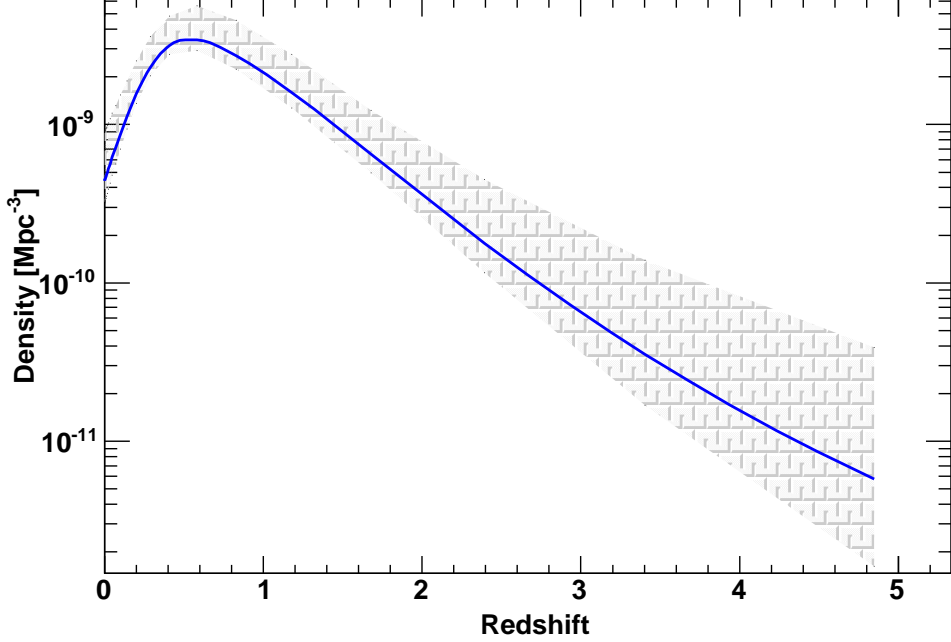


Fig. 15.— Number density of LAT-detected FSRQs as a function of redshift. The gray band represents the 1σ statistical uncertainty around the best-fit LF model.

be up to 15° off-axis (if these have low Doppler factors). *Fermi*-detected FSRQs represent only $\sim 0.1\%$ of the parent population for randomly pointed jets.

Monitoring observations with the Very Long Baseline Array (VLBA) established that LAT detected blazars have, on average, significantly faster apparent jet speeds than non-LAT detected blazars (Lister et al. 2009b; Savolainen et al. 2010). Their distribution of Lorentz factors is in good agreement with the results of our analysis. Moreover, they report the distribution of viewing angles with respect to the jet axis for FSRQs detected by LAT. From their study the average viewing angle is $2.9^\circ \pm 0.3^\circ$ and all the FSRQs in their sample have $\theta \leq 5^\circ$. There is thus substantial agreement within the VLBA monitoring observations and the results of our beaming model applied to γ -ray only data.

The space density of FR-II radio galaxies (i.e. the putative parent population of FSRQs) is reported to be $\sim 1580 \text{ Gpc}^{-3}$ (at 15 GHz) and $\sim 2200 \text{ Gpc}^{-3}$ (at 1.4 GHz) by Cara & Lister (2008) and Gendre et al. (2010) respectively. From our study we derive a space density of FSRQ parents of $\sim 1500 \text{ Gpc}^{-3}$ in substantial agreement with the numbers above.

Future work may test whether the intrinsic properties of blazars (i.e. Lorentz factor,

luminosity etc.) evolve with redshift. This will likely require larger complete samples and improved modeling of selections effects.

8.3. Spectral Energy Distribution

Blazars SEDs are characterized by the typical “two hump” spectrum where the low-energy peak is produced by electrons radiating via synchrotron and the high energy peak is produced via IC scattering off the same synchrotron photons (synchrotron-self Compton scenario; Maraschi et al. 1992) and/or external seed photons (external Compton scenario; Dermer & Schlickeiser 1993).

In this work we have combined quasi-simultaneous *Swift*/BAT and *Fermi*/LAT data to investigate the empirical properties of the IC component of the SEDs of the FSRQs detected by *Fermi*. All the SED show apparent curvature and have a peak somewhere in the 10 MeV–1 GeV band. There is no correlation between the IC peak luminosity and energy for the sample of FSRQs detected by *Fermi*. The existence of such correlation has been claimed in the past for the luminosity and the energy of the synchrotron peak (Ghisellini et al. 1998; Fossati et al. 1998) for a sample of blazars (i.e. FSRQs and BL Lacs). Thus it might be that this correlation (if real) exists only when the two families of blazars are joined together and that any correlation for the FSRQs class is washed away by the presence of the additional EC component. Also the lack of correlation of the IC peak luminosity and frequency reveals that FSRQs are, unlike BL Lacs, part of a population with homogenous properties.

We built average redshift-corrected SEDs in four different luminosity bins. The average SEDs are surprisingly similar as a function of luminosity (and redshift) as Fig. 9 testifies. Approximating the SED with a power law with an index 2.4, while not producing the correct shape, allows the reader to compute a k-correction useful up to redshift ≈ 2 . Beyond that this approximation is not valid.

8.4. The Contribution to the Diffuse Background

This work has important consequences for our understanding of the origins of the diffuse background. As pointed by several authors (e.g. Inoue & Totani 2009) and determined in this work, the spectrum of the diffuse emission arising from FSRQs shows curvature, due to the curved SEDs of these objects. We couple our model SED to our LF to predict the FSRQ contribution to the 10 keV to 100 GeV diffuse background. FSRQs produce $\sim 10\%$ of the cosmic diffuse emission in the 1 MeV-10 GeV band.

Because of its good sensitivity *Fermi* has already resolved as much as 50 % of the total flux from FSRQs in the 100 MeV–100 GeV band. Our analysis indicates that the contribution of *unresolved* FSRQs to the IGRB (Abdo et al. 2010d) is $9.66^{+1.67}_{-1.09} \times 10^{-7} \text{ ph cm}^{-2} \text{ s}^{-1} \text{ sr}^{-1}$ and thus only $9.3^{+1.6}_{-1.0} \%$ ($\pm 3 \%$ systematic uncertainty) of the intensity of the IGRB. This analysis is in good agreement with the results reported by Abdo et al. (2010e) except above 10 GeV where the use of a simple power law for the spectra of FSRQs was inadequate.

Our results appear in reasonably good agreement with those of Inoue et al. (2010) and of Inoue & Totani (2011), both in terms of spectral shape of the diffuse emission arising from FSRQs and its intensity. In their work, these authors rely on the sample of FSRQs and BL Lacs detected by EGRET. It is thus not surprising that their estimates of the contribution to the IGRB are slightly larger than ours. Finally, our estimate reported above is in good agreement with the results of Dermer (2007) that predicted that FSRQs would produce $\approx 10\text{--}15 \%$ of the γ -ray background.

LAT-detected FSRQs represent only $\sim 0.2 \%$ of the parent population (see § 7) and thus it is reasonable to expect that misaligned jets, although less luminous, but more numerous give a non-negligible contribution to the diffuse background. Our beaming model allowed us to explore this scenario. It is found that misaligned relativistic jets contribute $\sim 30 \%$ of the diffuse flux from the FSRQs class at redshift zero. If the Lorentz factor distribution does not change with redshift then the contribution of *unresolved* FSRQs and their misaligned siblings might be around $\sim 2.0 \times 10^{-6} \text{ ph cm}^{-2} \text{ s}^{-1}$ and thus $\sim 20 \%$ of the IGRB. Recently, Inoue & Totani (2011) predicted that radio galaxies of both the FR-I and FR-II type might be able to account for $\sim 25 \%$ of the intensity of the IGRB. In our work we found that FR-II alone could in principle (see above caveat) produce $\sim 10 \%$ of the IGRB. It can be envisaged that once also the contribution to the IGRB of BL Lacs and their parents will be established, the total γ -ray emission from relativistic jets might account for some $\sim 40\text{--}50 \%$ of the intensity of the IGRB.

Table 4. Parameters of the beaming models described in the text. Parameters without an error estimate were kept fixed during the fitting stage.

Parameter	Value	Value
k	-2.03 ± 0.70	-2.43 ± 0.11
k_1	$5.1 \pm 0.5^{\text{a}}$	$5.0 \pm 0.5^{\text{b}}$
B	3.04 ± 0.08	3.00 ± 0.08
γ_1	5	5
γ_2	40	40
\mathcal{L}_1	10^{40}	10^{38}
\mathcal{L}_2	10^{44}	10^{42}
p	4	5
χ^2/dof	1.3	1.5

^aIn units of 10^{-23} .

^bIn units of 10^{-26} .

A. Systematic Uncertainties

The sources of systematic uncertainties in this analysis are: incompleteness (i.e. missing redshifts), detection efficiency, blazar variability, and EBL. A detailed discussion of some of these problems was already given in Abdo et al. (2010e). Incompleteness in our sample is very small and introduces no appreciable systematic uncertainty as shown in § 4.3.

A.1. Detection Efficiency

The detection efficiency used to determine the sky area surveyed by *Fermi* at any given flux is very important in this analysis (see Abdo et al. 2010e, for a detailed discussion). The detection efficiency used in this work was derived in Abdo et al. (2010e) under the assumption that the blazars spectra can be approximated by a power law. While this might be true over a small energy band, it becomes a problematic assumption over the full 100 MeV–100 GeV band covered by the LAT. In this Section we estimate directly the systematic uncertainties connected to this hypothesis. We performed 3 end-to-end Monte Carlo simulations of the *Fermi* sky (see Abdo et al. 2010e, for details), assigning randomly a curved spectrum to each source. These spectra are extracted from a library created using the ~ 100 observed spectra derived in § 5 varying the parameters of the measured spectra within their errors. The simulations were then analyzed to derive the detection efficiency reported in Fig. 16. In particular in order to detect a source a maximum likelihood fit with a power law spectrum is performed. This is done in order to reproduce the inherent systematic uncertainty of fitting the curved spectrum of a source with a power law (Abdo et al. 2010a).

Fig. 16 shows the detection efficiency for a sample like that used in this analysis. Two aspects are noteworthy. First the efficiency at $F_{100} = 10^{-8} \text{ ph cm}^{-2} \text{ s}^{-1}$ (i.e. the lowest flux of this analysis by construction) is ~ 0.02 with a typical uncertainty of $\pm 5 \times 10^{-3}$ dictated by the small statistic in our simulations at the lowest fluxes. Second, at fluxes around $F_{100} \approx 10^{-7} \text{ ph cm}^{-2} \text{ s}^{-1}$ the detection efficiency becomes larger than 1.0. This effect is due to the fact that fitting a curved spectrum source with a power law yields to an overestimate of the source flux by a factor $\sim 10\%$ (see also Fig. 8 in Abdo et al. 2010e). Since Fig. 16 is built as the ratio (in a given bin) of the number of sources detected with a given flux to the number of simulated sources with that flux, the effect mentioned above leads to a detection efficiency > 1.0 .

In order to test the level of systematic uncertainty we derived the LF using the detection efficiency reported in Fig. 16. Given the “small” number of sources detected in the 3 simulations, it was not possible to derive a two-dimensional detection efficiency as a func-

tion of flux and spectral index (like that used in § 4 and derived for power law sources in Abdo et al. 2010e). For this reason the parameters of the distribution of photon indices of the FSRQ class cannot be derived from the analysis of the LF. As it is apparent from Table 3 most parameters of the LF derived in this section and those derived in § 4.2 are compatible within their statistical errors. The only parameter for which the difference is slightly larger than the statistical errors is α . The parameter α governs the trend of the redshift peak with luminosity and while its statistical error is in both case 0.03, the systematic error appears to be 0.05. This has very little impact on the analysis and the results of the previous sections are fully confirmed and robust against variations of the detection efficiency curve. As a further proof, the points of the de-evolved LF in Fig. 5 and Fig. 6 were computed using the detection efficiency of Fig. 16 while the shaded error region was computed using the model LF derived in § 4.2 that uses the detection efficiency for power law source.

We performed an additional test, by shifting the detection efficiency curve in Fig. 16 to fluxes 10 % brighter than measured. The rightward shift is most dramatic as it increases the magnitude of the correction at faint fluxes. The shift is performed in order to account for uncertainties in the determination of the detection efficiency. The parameters of the LF are all consistent within statistical uncertainty with those found in this and the previous sections and reported in Table 3. The index of the low-luminosity slope of the LF becomes slightly steeper (i.e. $\gamma_1=0.47\pm0.18$), and this yields a slightly larger contribution to the IGRB from FSRQs. We thus consider the typical systematic uncertainty connected to the estimate of the contribution to the IGRB to be $\sim 3\%$ of the IGRB 100 MeV–100 GeV intensity.

A.2. Variability

It is well known that blazars are inherently variable objects with variability in flux of up to a factor 10 or more. Throughout this work only average quantities (i.e. mean flux, mean luminosity and mean photon index) are used.

It is not straightforward to determine how blazar variability affects the analysis presented here. While the variability patterns and amplitudes of blazars as a class are still not known both Abdo et al. (2010c) and Abdo A., et al., (2011) presented a detailed analysis of the variability of the brightest *Fermi* blazars. They report that the variability amplitude of the FSRQ class is generally larger than that of the BL Lac population. However, most sources (either bright or faint ones) exceed their average flux for less than 5–20 % of the monitored time (i.e. respectively 11 months or 2 years). This drastically reduces the possibility that FSRQs (or blazars more in general) are detected because of a few bright flaring episodes. The effect of high-amplitude variability connected with a rising density of sources

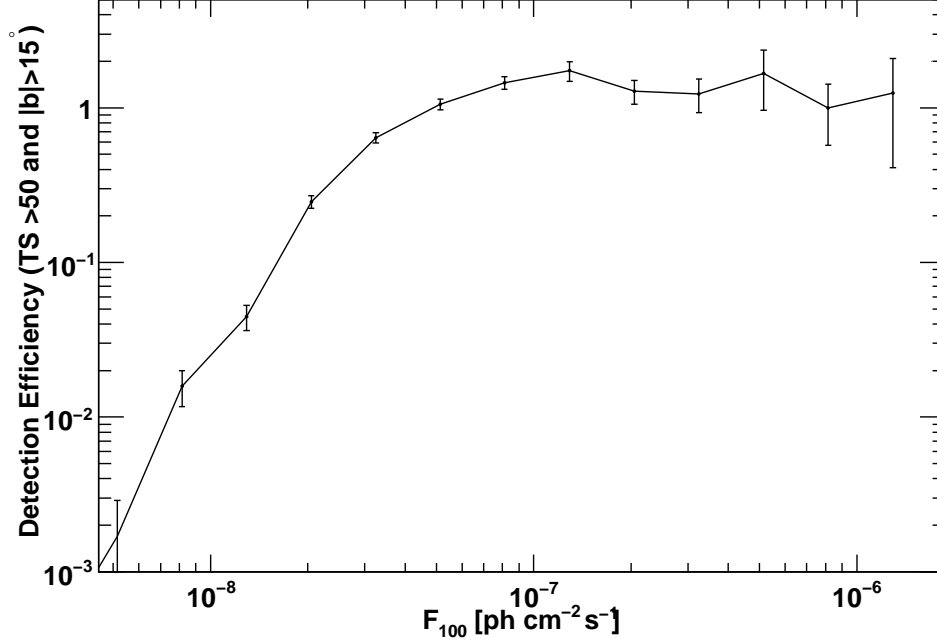


Fig. 16.— Detection efficiency as a function of flux for a population of sources with curved spectra similar to those of FSRQs determined in § 5.

at smaller flux might contaminate samples, as the one used here, with objects that formally should not be included. However, because of what reported above and the flatness of the FSRQs source count distribution (see Abdo et al. 2010e; Abdo A., et al., 2011, and Fig. 2) this effect is very likely marginal.

Another, smaller, problem is connected to the dependence of the effective area on the direction of the incoming photon and the LAT detector frame⁷. Short intense flares detected during favorable conditions (i.e. on axis and at azimuthal angles of ~ 0 , ~ 90 , ~ 180 , or ~ 270 degrees) might lead to a higher TS, increasing the likelihood of source detection. However, because of *Fermi*'s continuous scanning of the sky and because most flares are observed to last 10 days or longer (Abdo et al. 2010c), the effect above has negligible influence on the analysis presented here.

Finally, we believe that variability does not hamper the results of this analysis. Using even longer integration times (e.g. 2, or 3 years) will be the most efficient way to confirm

⁷See e.g. http://www.slac.stanford.edu/exp/glast/groups/canda/lat_Performance.htm and Atwood et al. (2009).

the results of this analysis and dilute the effect of blazar variability.

A.3. Extragalactic Background Light

Uncertainty in the level of the EBL, in particular at medium to high redshift, might in principle affect our analysis. Energetic γ -rays from FSRQs at high redshifts might be absorbed by the EBL and if this effect is not taken into account the source-frame luminosity would be underestimated. This would lead to wrong estimates of the space densities of FSRQs. However we believe this uncertainty is negligible.

The uncertainty in the level of the EBL would impact the estimate of the k-correction which allows us to determine the source-frame luminosities. As shown in Fig. 10, neglecting the EBL at once and adopting a simple power-law spectrum with a photon index of 2.4 (instead of the average SED determined in § 5) introduces an uncertainty of $\leq 4\%$ on the value of the k-correction at $z=3$. Since all the *Fermi* FSRQs are detected within this redshift, this uncertainty produces no appreciable impact on the determination of the luminosity function.

MA acknowledges Y. Inoue and T. Venters for providing their data in electronic form and for interesting discussions about the origin of the IGRB. MA acknowledges support from NASA grant NNH09ZDA001N for the study of the origin of the IGRB. RWR acknowledges NASA grant NNX08AW30G and extensive consultation with the OVRO Fermi group.

The *Fermi* LAT Collaboration acknowledges generous ongoing support from a number of agencies and institutes that have supported both the development and the operation of the LAT as well as scientific data analysis. These include the National Aeronautics and Space Administration and the Department of Energy in the United States, the Commissariat à l’Energie Atomique and the Centre National de la Recherche Scientifique / Institut National de Physique Nucléaire et de Physique des Particules in France, the Agenzia Spaziale Italiana and the Istituto Nazionale di Fisica Nucleare in Italy, the Ministry of Education, Culture, Sports, Science and Technology (MEXT), High Energy Accelerator Research Organization (KEK) and Japan Aerospace Exploration Agency (JAXA) in Japan, and the K. A. Wallenberg Foundation, the Swedish Research Council and the Swedish National Space Board in Sweden. Additional support for science analysis during the operations phase is gratefully acknowledged from the Istituto Nazionale di Astrofisica in Italy and the Centre National d’Études Spatiales in France.

Facilities: Fermi/LAT, Swift/BAT

REFERENCES

- Abdo, A. A., et al. 2009, ApJ, 700, 597
- . 2010a, ApJS, 188, 405
- . 2010b, ApJ, 720, 912
- . 2010c, ApJ, 722, 520
- . 2010d, Physical Review Letters, 104, 101101
- . 2010e, ApJ, 720, 435
- . 2010f, ApJ, 715, 429
- Abdo, A., e. a. 2011, eprint arXiv:1108.1435
- Abdo A., et al.,. 2011, ArXiv e-prints
- Aird, J., et al. 2010, MNRAS, 401, 2531

- Ajello, M., Greiner, J., Kanbach, G., Rau, A., Strong, A. W., & Kennea, J. A. 2008a, *ApJ*, 678, 102
- Ajello, M., Rebusco, P., Cappelluti, N., Reimer, O., Böhringer, H., La Parola, V., & Cusumano, G. 2010, *ApJ*, 725, 1688
- Ajello, M., et al. 2008b, *ApJ*, 689, 666
- . 2008c, *ApJ*, 673, 96
- . 2009a, *ApJ*, 690, 367
- . 2009b, *ApJ*, 699, 603
- Atwood, W. B., et al. 2009, *ApJ*, 697, 1071
- Avni, Y. 1976, *ApJ*, 210, 642
- Barthelmy, S. D., et al. 2005, *Space Science Reviews*, 120, 143
- Beckmann, V., Engels, D., Bade, N., & Wucknitz, O. 2003, *A&A*, 401, 927
- Begelman, M. C., Volonteri, M., & Rees, M. J. 2006, *MNRAS*, 370, 289
- Bhattacharya, D., Sreekumar, P., & Mukherjee, R. 2009, *Research in Astronomy and Astrophysics*, 9, 85
- Blandford, R. D., & Znajek, R. L. 1977, *MNRAS*, 179, 433
- Caccianiga, A., Maccacaro, T., Wolter, A., Della Ceca, R., & Gioia, I. M. 2002, *ApJ*, 566, 181
- Cara, M., & Lister, M. L. 2008, *ApJ*, 674, 111
- Chiang, J., Fichtel, C. E., von Montigny, C., Nolan, P. L., & Petrosian, V. 1995, *ApJ*, 452, 156
- Chiang, J., & Mukherjee, R. 1998, *ApJ*, 496, 752
- Cowie, L. L., Songaila, A., & Barger, A. J. 1999, *AJ*, 118, 603
- Croton, D. J., et al. 2006, *MNRAS*, 365, 11
- Cusumano, G., et al. 2010, *A&A*, 524, A64+
- Della Ceca, R., et al. 2008, *A&A*, 487, 119

- Dermer, C. D. 1995, *ApJ*, 446, L63+
- . 2007, *ApJ*, 659, 958
- Dermer, C. D., & Schlickeiser, R. 1993, *ApJ*, 416, 458
- Di Matteo, T., Springel, V., & Hernquist, L. 2005, *Nature*, 433, 604
- Dotti, M., Colpi, M., Haardt, F., & Mayer, L. 2007, *MNRAS*, 379, 956
- Dunlop, J. S., & Peacock, J. A. 1990, *MNRAS*, 247, 19
- Escala, A., Larson, R. B., Coppi, P. S., & Mardones, D. 2004, *ApJ*, 607, 765
- Fakhouri, O., Ma, C.-P., & Boylan-Kolchin, M. 2010, *MNRAS*, 406, 2267
- Fan, X., et al. 2003, *AJ*, 125, 1649
- Fichtel, C. E., Hartman, R. C., Kniffen, D. A., Thompson, D. J., Ogelman, H., Ozel, M. E., Tumer, T., & Bignami, G. F. 1975, *ApJ*, 198, 163
- Fossati, G., Maraschi, L., Celotti, A., Comastri, A., & Ghisellini, G. 1998, *MNRAS*, 299, 433
- Franceschini, A., Rodighiero, G., & Vaccari, M. 2008, *A&A*, 487, 837
- Gehrels, N., et al. 2004, *ApJ*, 611, 1005
- Gendre, M. A., Best, P. N., & Wall, J. V. 2010, *MNRAS*, 404, 1719
- Ghisellini, G., Celotti, A., Fossati, G., Maraschi, L., & Comastri, A. 1998, *MNRAS*, 301, 451
- Ghisellini, G., Tavecchio, F., & Ghirlanda, G. 2009, *MNRAS*, 399, 2041
- Giommi, P., & Padovani, P. 1994, *MNRAS*, 268, L51
- Hartman, R. C., et al. 1999, *ApJS*, 123, 79
- Hasinger, G., Miyaji, T., & Schmidt, M. 2005, *A&A*, 441, 417
- Hogg, D. W. 1999, *ArXiv:astro-ph/9905116*
- Hopkins, A. M., & Beacom, J. F. 2006, *ApJ*, 651, 142
- Inoue, Y. 2011, *ApJ*, 733, 66

- Inoue, Y., & Totani, T. 2009, *ApJ*, 702, 523
- . 2011, *ApJ*, 728, 73
- Inoue, Y., Totani, T., & Mori, M. 2010, *PASJ*, 62, 1005
- Kauffmann, G., & Haehnelt, M. 2000, *MNRAS*, 311, 576
- Keshet, U., Waxman, E., & Loeb, A. 2004, *J. Cosmology Astropart. Phys.*, 4, 6
- Kraushaar, W. L., Clark, G. W., Garmire, G. P., Borken, R., Higbie, P., Leong, V., & Thorsos, T. 1972, *ApJ*, 177, 341
- Kulkarni, G., & Loeb, A. 2011, *ArXiv:1107.051*
- La Franca, F., & Cristiani, S. 1997, *AJ*, 113, 1517
- La Franca, F., et al. 2005, *ApJ*, 635, 864
- Lähteenmäki, A., & Valtaoja, E. 2003, *ApJ*, 590, 95
- Lister, M. L. 2003, *ApJ*, 599, 105
- Lister, M. L., Homan, D. C., Kadler, M., Kellermann, K. I., Kovalev, Y. Y., Ros, E., Savolainen, T., & Zensus, J. A. 2009a, *ApJ*, 696, L22
- Lister, M. L., & Marscher, A. P. 1997, *ApJ*, 476, 572
- Lister, M. L., et al. 2009b, *AJ*, 138, 1874
- Maraschi, L., Ghisellini, G., & Celotti, A. 1992, *ApJ*, 397, L5
- Marshall, H. L., Tananbaum, H., Avni, Y., & Zamorani, G. 1983, *ApJ*, 269, 35
- Mayer, L., Kazantzidis, S., Escala, A., & Callegari, S. 2010, *Nature*, 466, 1082
- Merloni, A. 2004, *MNRAS*, 353, 1035
- Miyaji, T., Hasinger, G., & Schmidt, M. 2001, *A&A*, 369, 49
- Mücke, A., & Pohl, M. 2000, *MNRAS*, 312, 177
- Narumoto, T., & Totani, T. 2006, *ApJ*, 643, 81
- Nieppola, E., Valtaoja, E., Tornikoski, M., Hovatta, T., & Kotiranta, M. 2008, *A&A*, 488, 867

- Padovani, P., Giommi, P., Landt, H., & Perlman, E. S. 2007, *ApJ*, 662, 182
- Rector, T. A., Stocke, J. T., Perlman, E. S., Morris, S. L., & Gioia, I. M. 2000, *AJ*, 120, 1626
- Romani, R. W. 2006, *AJ*, 132, 1959
- Sanders, D. B., Soifer, B. T., Elias, J. H., Madore, B. F., Matthews, K., Neugebauer, G., & Scoville, N. Z. 1988, *ApJ*, 325, 74
- Savolainen, T., Homan, D. C., Hovatta, T., Kadler, M., Kovalev, Y. Y., Lister, M. L., Ros, E., & Zensus, J. A. 2010, *A&A*, 512, A24+
- Schmidt, M. 1968, *ApJ*, 151, 393
- Schmidt, M., Schneider, D. P., & Gunn, J. E. 1995, *AJ*, 110, 68
- Silverman, J. D., et al. 2008, *ApJ*, 679, 118
- Sreekumar, P., et al. 1998, *ApJ*, 494, 523
- Stecker, F. W., Malkan, M. A., & Scully, S. T. 2006, *ApJ*, 648, 774
- Stecker, F. W., & Salamon, M. H. 1996, *ApJ*, 464, 600
- Stecker, F. W., & Venters, T. M. 2010, *ArXiv e-prints*
- Tueller, J., Mushotzky, R. F., Barthelmy, S., Cannizzo, J. K., Gehrels, N., Markwardt, C. B., Skinner, G. K., & Winter, L. M. 2007, *ArXiv e-prints*, 711
- Ueda, Y., Akiyama, M., Ohta, K., & Miyaji, T. 2003, *ApJ*, 598, 886
- Urry, C. M., & Padovani, P. 1991, *ApJ*, 371, 60
- Urry, C. M., & Shafer, R. A. 1984, *ApJ*, 280, 569
- Volonteri, M., & Rees, M. J. 2005, *ApJ*, 633, 624
- Wall, J. 2008, *ArXiv:0807.3792*
- Wall, J. V., Jackson, C. A., Shaver, P. A., Hook, I. M., & Kellermann, K. I. 2005, *A&A*, 434, 133
- Willott, C. J., et al. 2010, *AJ*, 139, 906
- Wolter, A., & Celotti, A. 2001, *A&A*, 371, 527

Wyithe, J. S. B., & Loeb, A. 2003, ApJ, 595, 614